Discontinuous Galerkin methods for the simulation of the propagation of the elastic wave equations in the frequency domain

Marie Bonnasse-Gahot, Henri Calandra, Julien Diaz, Stéphane Lanteri

To cite this version:

Marie Bonnasse-Gahot, Henri Calandra, Julien Diaz, Stéphane Lanteri. Discontinuous Galerkin methods for the simulation of the propagation of the elastic wave equations in the frequency domain. [Research Report] RR-8989, INRIA Bordeaux; INRIA Sophia Antipolis - Méditerranée. 2015, pp.56. hal-01408700v1

HAL Id: hal-01408700
https://inria.hal.science/hal-01408700v1

Submitted on 5 Dec 2016 (v1), last revised 13 Dec 2016 (v2)

Discontinuous Galerkin methods for the simulation of the propagation of the elastic wave equations in the frequency domain

Marie Bonnasse-Gahot, Henri Calandra, Julien Diaz, Stéphane Lanteri

RESEARCH REPORT
N° 8989
April 2015
Project-Teams Magique 3D and Nachos

ISSN 0249-6399 ISRN INRIA/RR--8989--FR+ENG

Discontinuous Galerkin methods for the simulation of the propagation of the elastic wave equations in the frequency domain

Marie Bonnasse-Gahot*[†], Henri Calandra[‡], Julien Diaz*,
Stéphane Lanteri [†]

Project-Teams Magique 3D and Nachos

Research Report n° 8989 — April 2015 — 53 pages

Abstract: In this report, we study two nodal discontinuous Galerkin (DG) methods, the centered flux DG method and the upwind flux DG method, for the resolution of the 2D elastic waves equations in frequency domain, so called Helmholtz equations. We give the formulation of both methods and we compare the obtained results.

Key-words: seismic imaging, forward problem, frequency domain, elastic waves, centered flux DG method, upwind flux DG method, discontinuous Galerkin method

---

* EPI Magique 3D INRIA Bordeaux-Sud-Ouest
[†] EPI Nachos INRIA Sophia Antipolis-Méditerranée
[‡] TOTAL Exploration-Production

**RESEARCH CENTRE
BORDEAUX – SUD-OUEST**

200 avenue de la Vieille Tour
33405 Talence Cedex

Méthodes de Galerkine discontinues pour la résolution des équations d'Helmholtz élastiques en domaine fréquentiel

Résumé : Dans ce rapport, nous étudions deux méthodes de Galerkine discontinues (GD), la méthode GD à flux centrés et la méthode GD à flux décentrés, pour la résolution des équations 2D des ondes élastiques en domaine fréquentiel, appelées aussi équations d'Helmholtz élastiques. Nous présentons la formulation des deux méthodes et nous comparons les résultats numériques obtenus.

Mots-clés : imagerie sismique, résolution du problème direct, domain fréquentiel,ondes élastiques, méthodes de Galerkin discontinues, méthode GD à flux centrés, méthode GD à flux décentrés

Contents

1 Introduction

The numerical solution of wave equations (acoustics, elastodynamics or electromagnetics) is increasingly used in many areas such as civil engineering, mechanical engineering, aerospace engineering, geophysics, medicine, biology or telecommunications. Applications are then various: noise reduction, radar and antenna design, satellites and waveguides, detection of hidden targets, medical imaging, seismic imaging, earthquakes dynamics, etc.

The scientific context of the present study is seismic imaging, which aims at recovering the structure of the earth. A seismic imaging method using a wave equation model is called a *seismic-reflection technique*. It is the most used imaging method in the petroleum industry because it is the one that yields the most accurate images of the subsurface in view of analyzing them to find hydrocarbons.

The principle of a seismic acquisition is simple: sources, generally placed on the top of the subsurface, emit waves inside the earth; then receivers, which can be placed at the top or in the depth, record the reflected waves (arrival time and amplitude). The amplitudes of reflected fields allow to recover the material characteristics constituting the ground, and the arrival times allow to establish where the reflectors are. Reflectors are the interfaces between two different media.

Seismic imaging campaigns can be done in the sea or in the ground and with its results, one can construct a card that represents the variations of the velocity in the medium. The latter is referred to as the velocity model. Its quality depends on the number of sources used. It is the reason why in seismic imaging the number of sources used is usually large (about 1000).

Consequently, the efficiency of the whole procedure is directly related to the efficiency of the numerical method used to solve the wave equations.

There exists several seismic imaging methods: the Reverse Time Migration (RTM) and the Full Wave Inversion (FWI) are the most widely used. Both methods are based on the resolution of wave equations.

The RTM uses the fact that the wave equations are reversible. From the sources, one propagates waves to obtain the propagated field. Then one makes use of the recorded data of the reflected waves as initial data, and propagates them in order to obtain the retro-propagated field. Finally the image of the subsurface is obtained by correlating the propagated fields and retro-propagated fields: at each point where there is a correlation, a reflector is deduced.

The FWI is an iterative procedure solving $2N$ harmonic wave equations at each iteration of the algorithm if N sources are used. It defines an inversion process (see [1] for more details about inversion process), and thus it is composed of two major steps: first, one solves the forward problem (i.e. the propagation of the wave equations) which models the phenomenon for each source; then, one computes residuals thanks to a comparison between the recorded data and the numerical data using, e.g., a least-squares method. These residuals are used to update the velocity and the process is repeated until there is accordance between recorded data and numerical data.

Seismic imaging can be performed in the time-domain or in the frequency-domain. Time-domain approaches do not require an important computational cost, but the implementation of the imaging condition is more complicated than in the frequency-domain case. Furthermore, in frequency-domain approaches, it is not necessary to store the solution at each time step of the forward simulation. This is interesting because seismic imaging involves very large problems with a lot of data. Memory must be used with attention. In the frequency-domain case, the main drawback then lies in the need to solve a large linear system of equations which represents a challenging task when considering realistic 3D elastic media, despite the recent advances on high performance computing.

In this context, we are interesting in the modeling part, i.e. the resolution of the forward problem of the FWI, assuming a time-harmonic regime, leading to the so-called Helmholtz equations. The main objective of our work is to propose and develop a new finite element type solver characterized by a reduced-size discrete operator (as compared to existing such solvers) without hampering the accuracy of the numerical solution.

A wide variety of approximation methods of the wave equations is currently available. Moreover, with the progress of high performance computing, it is now possible to model elastic domain. The FWI is performed with methods belonging to the family of finite difference (FD) method or finite element (FE) methods. FD methods use regular grid and allow to obtain easier systems to solve (as compared to FE methods). But they may lack of sufficient accuracy when one considers a highly heterogeneous medium or when the underlying mesh is too coarse. Moreover with FD methods, one does not take into account the irregular topography of the subsurface because the structured mesh can not correctly approach interfaces. Indeed, with Cartesian meshes, it is difficult to handle a steep subsurface.

By contrast, with FE methods, one can use unstructured meshes to discretize accurately complex domains. One inherits from a greater flexibility in the construction of the mesh. However, FE methods require more memory space than FD methods. Two kinds of FE methods seem to be adapted to wave propagation simulation: spectral elements (SE) methods and discontinuous Galerkin (DG) methods (see [2] for a comparison between DG methods and finite differences methods applied to wave equations for seismic applications).

SE methods use high order functions and need less memory space than classical FE methods without hampering the numerical convergence order. However, SE methods are formulated on quadrangular (2D case)/hexahedral (3D case) meshes which may not be ideally adapted to the discretization of complex geometries in the 3D case. DG methods and FE methods mainly differ on basis functions: DG basis functions are only piecewise continuous. Moreover in addition to the fact that they are formulated on unstructured triangular meshes, they are more suitable than continuous Galerkin (CG) methods to deal with *hp*-adaptivity (interpolation degree p or mesh step h can change from element to another), providing a greater flexibility in the mesh construction and the discretization of the different regions of the subsurface. For time-domain problems, DG methods provide explicit representation of the solution because the mass matrix is block diagonal. In addition, they are nicely adapted to high performance computing.

With the goal to develop more accurate, more efficient and cheaper forward solvers, we are interested here in solving the elastic Helmholtz equations with DG methods. In his doctoral thesis, R. Brossier [3] applied the centered flux DG method to the elastic Helmholtz equations under a pseudo-conservative form. In this study we study numerically a centered flux DG method which is an adaptation of the method studied by S. Delcourte *et al.* in [4] in the time-domain case, and an upwind flux DG method formulated as in [5] for the time-harmonic Maxwell equations. We note that Käser and Dumbser in [6] have also considered an upwind flux DG formulation for time-domain elastic wave equations.

This report describes a preliminary study in view of the development a new class of DG methods, the hybridizable DG method, which will be the subject of a second document where we will in particular compare results obtained with upwind DG method and the new HDG method.

2 Problem statement and notations

2.1 Isotropic elastodynamics system

We consider the first order formulation of the elastodynamics system assuming a time-harmonic regime. In the 3D case, for $\mathbf{x} = (x, y, z) \in \Omega \subset \mathbb{R}^3$, this systems reads as

$$\left\{ \begin{array}{lcll} i\omega\rho(\mathbf{x})\mathbf{v}(\mathbf{x}) & = & \nabla \cdot \underline{\underline{\sigma}}(\mathbf{x}) + f(\mathbf{x}) & \text{in } \Omega, \\ i\omega\underline{\underline{\sigma}}(\mathbf{x}) & = & \underline{\underline{C}}(\mathbf{x})\ \underline{\underline{\epsilon}}(\mathbf{v}(\mathbf{x})) & \text{in } \Omega, \end{array} \right. \tag{2.1}$$

where i is the imaginary unit, ω the angular frequency, $\rho(\mathbf{x})$ is the mass density and $f(\mathbf{x})$ is the source term (volumetric forces). Moreover, $\mathbf{v}(\mathbf{x}) = (v_x(\mathbf{x}), v_y(\mathbf{x}), v_z(\mathbf{x})^T$ is the velocity vector, $\underline{\underline{\epsilon}}$ is the stress tensor, with $\epsilon_{ij} = \dfrac{1}{2}\left(\dfrac{\partial v_i}{\partial j} + \dfrac{\partial v_j}{\partial i}\right), \quad i, j = x, y, z$, $\underline{\underline{\sigma}}$ is the stain tensor with, in the isotropic case, $\sigma_{ij} = \lambda\delta_{ij}\mathrm{Tr}(\underline{\underline{\epsilon}}) + 2\mu\epsilon_{ij}, \quad i, j = x, y, z$ and $\underline{\underline{C}}$ is a $3 \times 3 \times 3 \times 3$ symetric fourth order tensor, with elastic coefficients. Using Voigt's notation, $\underline{\underline{C}}$ can be reduced to 6×6 matrix. Using

$$\begin{aligned} ij \to \alpha \text{ or } kl \to \beta = & 11 \to 1 \\ & 22 \to 2 \\ & 33 \to 3 \\ & 12 \to 4 \\ & 23 \to 5 \\ & 13 \to 6 \end{aligned}$$

we have that in the isotropic case

$$\underline{\underline{C}}(\mathbf{x}) = \begin{pmatrix} \lambda(\mathbf{x}) + 2\mu(\mathbf{x}) & \lambda(\mathbf{x}) & \lambda(\mathbf{x}) & 0 & 0 & 0 \\ \lambda(\mathbf{x}) & \lambda(\mathbf{x}) + 2\mu(\mathbf{x}) & \lambda(\mathbf{x}) & 0 & 0 & 0 \\ \lambda(\mathbf{x}) & \lambda(\mathbf{x}) & \lambda(\mathbf{x}) + 2\mu(\mathbf{x}) & 0 & 0 & 0 \\ 0 & 0 & 0 & \mu(\mathbf{x}) & \mu(\mathbf{x}) & 0 \\ 0 & 0 & 0 & 0 & \mu(\mathbf{x}) & \mu(\mathbf{x}) \\ 0 & 0 & 0 & \mu(\mathbf{x}) & 0 & \mu(\mathbf{x}) \end{pmatrix},$$

where λ and μ are the Lamé's coefficients.

The boundary conditions are given by

$$\left\{ \begin{array}{ll} \underline{\underline{\sigma}}\mathbf{n} & = 0 \text{ on } \Gamma_a, \\ (\mathbf{D_n})^- \, \mathbf{W} & = 0 \text{ on } \Gamma_b, \end{array} \right. \tag{2.2}$$

with $\Gamma_a \cup \Gamma_b = \partial\Omega$ and $\Gamma_a \cap \Gamma_b = \emptyset$. The first relation of (2.2) describes a free surface condition on Γ_a while the second relation indicates an absorbing boundary condition on Γ_b that we will detail in section 3.1.4.

Thereafter, to simplify, we omit the spatial-dependency in the physical parameters ρ, λ and μ, tensors $\underline{\underline{C}}, \underline{\underline{\sigma}}$ and $\underline{\underline{\epsilon}}$ and vector $\mathbf{v}$. We can develop the equations of system (2.1) and obtain

$$\left\{\begin{array}{lcl}
i\omega V_x & = & \dfrac{1}{\rho}\left(\dfrac{\partial \sigma_{xx}}{\partial x}+\dfrac{\partial \sigma_{xy}}{\partial y}+\dfrac{\partial \sigma_{xz}}{\partial z}\right), \\
i\omega V_y & = & \dfrac{1}{\rho}\left(\dfrac{\partial \sigma_{xy}}{\partial x}+\dfrac{\partial \sigma_{yy}}{\partial y}+\dfrac{\partial \sigma_{yz}}{\partial z}\right), \\
i\omega V_z & = & \dfrac{1}{\rho}\left(\dfrac{\partial \sigma_{xz}}{\partial x}+\dfrac{\partial \sigma_{yz}}{\partial y}+\dfrac{\partial \sigma_{zz}}{\partial z}\right), \\
i\omega \sigma_{xx} & = & (\lambda+2\mu)\dfrac{\partial V_x}{\partial x}+\lambda\left(\dfrac{\partial V_y}{\partial y}+\dfrac{\partial V_z}{\partial z}\right), \\
i\omega \sigma_{yy} & = & (\lambda+2\mu)\dfrac{\partial V_y}{\partial y}+\lambda\left(\dfrac{\partial V_x}{\partial x}+\dfrac{\partial V_z}{\partial z}\right), \\
i\omega \sigma_{zz} & = & (\lambda+2\mu)\dfrac{\partial V_z}{\partial z}+\lambda\left(\dfrac{\partial V_y}{\partial y}+\dfrac{\partial V_x}{\partial x}\right), \\
i\omega \sigma_{xy} & = & \mu\left(\dfrac{\partial V_x}{\partial y}+\dfrac{\partial V_y}{\partial x}\right), \\
i\omega \sigma_{yz} & = & \mu\left(\dfrac{\partial V_z}{\partial y}+\dfrac{\partial V_y}{\partial z}\right), \\
i\omega \sigma_{xz} & = & \mu\left(\dfrac{\partial V_x}{\partial z}+\dfrac{\partial V_z}{\partial x}\right).
\end{array}\right. \tag{2.3}$$

In 2D, the y components do not exist and we only have a system of 5 equations with 5 unknowns

$$\left\{\begin{array}{lcl}
i\omega V_x & = & \dfrac{1}{\rho}\left(\dfrac{\partial \sigma_{xx}}{\partial x}+\dfrac{\partial \sigma_{xz}}{\partial z}\right), \\
i\omega V_z & = & \dfrac{1}{\rho}\left(\dfrac{\partial \sigma_{xz}}{\partial x}+\dfrac{\partial \sigma_{zz}}{\partial z}\right), \\
i\omega \sigma_{xx} & = & (\lambda+2\mu)\dfrac{\partial V_x}{\partial x}+\dfrac{\partial V_z}{\partial z}, \\
i\omega \sigma_{zz} & = & (\lambda+2\mu)\dfrac{\partial V_z}{\partial z}+\dfrac{\partial V_x}{\partial x}, \\
i\omega \sigma_{xz} & = & \mu\left(\dfrac{\partial V_x}{\partial z}+\dfrac{\partial V_z}{\partial x}\right).
\end{array}\right. \tag{2.4}$$

2.1.1 Vectorial form

We can rewrite system (2.3) under a vectorial form

$$i\omega \mathbf{W}+\mathbf{A}_x\frac{\partial \mathbf{W}}{\partial x}+\mathbf{A}_y\frac{\partial \mathbf{W}}{\partial y}+\mathbf{A}_z\frac{\partial \mathbf{W}}{\partial z}=0, \tag{2.5}$$

with

$$\mathbf{W}=\left(V_x, V_y, V_z, \sigma_{xx}, \sigma_{yy}, \sigma_{zz}, \sigma_{xy}, \sigma_{yz}, \sigma_{xz}\right)^T,$$

$$\mathbf{A}_x = -\begin{pmatrix} 0 & 0 & 0 & \frac{1}{\rho} & 0 & 0 & 0 & 0 & 0 \\ 0 & 0 & 0 & 0 & 0 & 0 & \frac{1}{\rho} & 0 & 0 \\ 0 & 0 & 0 & 0 & 0 & 0 & 0 & 0 & \frac{1}{\rho} \\ \lambda+2\mu & 0 & 0 & 0 & 0 & 0 & 0 & 0 & 0 \\ \lambda & 0 & 0 & 0 & 0 & 0 & 0 & 0 & 0 \\ \lambda & 0 & 0 & 0 & 0 & 0 & 0 & 0 & 0 \\ 0 & \mu & 0 & 0 & 0 & 0 & 0 & 0 & 0 \\ 0 & 0 & 0 & 0 & 0 & 0 & 0 & 0 & 0 \\ 0 & 0 & \mu & 0 & 0 & 0 & 0 & 0 & 0 \end{pmatrix}, \quad \mathbf{A}_y = -\begin{pmatrix} 0 & 0 & 0 & 0 & 0 & 0 & \frac{1}{\rho} & 0 & 0 \\ 0 & 0 & 0 & 0 & \frac{1}{\rho} & 0 & 0 & 0 & 0 \\ 0 & 0 & 0 & 0 & 0 & 0 & 0 & \frac{1}{\rho} & 0 \\ 0 & \lambda & 0 & 0 & 0 & 0 & 0 & 0 & 0 \\ 0 & \lambda+2\mu & 0 & 0 & 0 & 0 & 0 & 0 & 0 \\ 0 & \lambda & 0 & 0 & 0 & 0 & 0 & 0 & 0 \\ \mu & 0 & 0 & 0 & 0 & 0 & 0 & 0 & 0 \\ 0 & 0 & \mu & 0 & 0 & 0 & 0 & 0 & 0 \\ 0 & 0 & 0 & 0 & 0 & 0 & 0 & 0 & 0 \end{pmatrix},$$

$$\mathbf{A}_z = -\begin{pmatrix} 0 & 0 & 0 & 0 & 0 & 0 & 0 & 0 & \frac{1}{\rho} \\ 0 & 0 & 0 & 0 & 0 & 0 & 0 & \frac{1}{\rho} & 0 \\ 0 & 0 & 0 & 0 & 0 & \frac{1}{\rho} & 0 & 0 & 0 \\ 0 & 0 & \lambda & 0 & 0 & 0 & 0 & 0 & 0 \\ 0 & 0 & \lambda & 0 & 0 & 0 & 0 & 0 & 0 \\ 0 & 0 & \lambda+2\mu & 0 & 0 & 0 & 0 & 0 & 0 \\ 0 & 0 & 0 & 0 & 0 & 0 & 0 & 0 & 0 \\ 0 & \mu & 0 & 0 & 0 & 0 & 0 & 0 & 0 \\ \mu & 0 & 0 & 0 & 0 & 0 & 0 & 0 & 0 \end{pmatrix}.$$

2.1.2 Notations

We discretize the computational domain Ω in a collection of disjoint elements (tetrahedrons for the 3D case, triangles for the 2D case) $\mathcal{T}_h$. We denote by

- $\mathcal{F}(K)$ the set of faces (edges in the 2D case, anyhow, we call it face) of an element K,
- F a face of an element K,
- $\mathcal{F}_b$ the union of all boundary faces F_b, i.e. $F_b = \partial K \cap \partial\Omega$,
- $\mathcal{F}_i$ the union of all interior faces F_i i.e. $F_i = \partial K \cap \partial K'$ where K and K' are neighbourgs,
- $\mathcal{F}_h$ the set of all faces $\mathcal{T}_h$, i.e. $\mathcal{F}_h = \mathcal{F}_i \cup \mathcal{F}_b$,
- $\mathbf{n}$ the outward unit norm vector to K, $\mathbf{n}'$ the outward unit norm vector to K'.

We define the *jump* $[\![\cdot]\!]$ and the *mean (average)* $\{\cdot\}$ such as

- On a face $F \in \mathcal{F}_i$, the jump $[\![\cdot]\!]$ of a vector $\mathbf{u}$ is

  $$[\![\mathbf{u}\cdot\mathbf{n}]\!] = \mathbf{u}^K \cdot \mathbf{n} + \mathbf{u}^{K'} \cdot \mathbf{n}' = \mathbf{u}^K \cdot \mathbf{n} - \mathbf{u}^{K'} \cdot \mathbf{n},$$

  and the jump of a tensor $\underline{\underline{\sigma}}$ is

  $$[\![\underline{\underline{\sigma}}\cdot\mathbf{n}]\!] = \underline{\underline{\sigma}}^K \mathbf{n} + \underline{\underline{\sigma}}^{K'} \mathbf{n}' = \underline{\underline{\sigma}}^K \mathbf{n} - \underline{\underline{\sigma}}^{K'} \mathbf{n}.$$

- On a face $F \in \mathcal{F}_b$, the jump $[\![\cdot]\!]$ of $\mathbf{u}$ is

$$[\![\mathbf{u} \cdot \mathbf{n}]\!] = \mathbf{u}^K \cdot \mathbf{n},$$

  and for $\underline{\underline{\sigma}}$

$$[\![\underline{\underline{\sigma}} \cdot \mathbf{n}]\!] = \underline{\underline{\sigma}}^K \mathbf{n}.$$

- On a face $F \in \mathcal{F}_i$, the average $\{\cdot\}$ of a scalar variable u is

$$\{u\} = \frac{u^K + u^{K'}}{2},$$

  and for a vector $\mathbf{u}$

$$\{\mathbf{u}\} = \frac{\mathbf{u}^K + \mathbf{u}^{K'}}{2}.$$

- On a face $F \in \mathcal{F}_b$, we have for u

$$\{u\} = u^K,$$

  and for $\mathbf{u}$

$$\{\mathbf{u}\} = \mathbf{u}^K.$$

Let $\mathbb{P}_p(D)$ denote the space of polynomial functions of degree at most p on domain D. For any element K of $\mathcal{T}_h$, $\Phi^K = \left(\varphi^K\right)_i$, $i = 1, df_K$, is a basis of $\mathbb{P}_p(K)$ with Lagrange's polynomial functions; df_K is the number of degrees of freedom (ndof) with $df_K = \dfrac{(p+s)!}{s!}$ with s the space dimension, and

$$\varphi_i^K \in \mathbb{P}_p, \varphi_i^K(a_j) = \delta_{ij}, \qquad 1 \leq j \leq df_K,$$

where δ_{ij} is Kronecker symbol and a_j coordinates of the j^{th} K dof. We define the following finite elements spaces

$$V_h = \{v_h \in L^2(\Omega) | \forall K \in \mathcal{T}_h, v_h|_K \in \mathbb{P}_p(K)\},$$

$$\mathbf{V}_h = \{\mathbf{v}_h \in \left(L^2(\Omega)\right)^3 | \forall K \in \mathcal{T}_h, \mathbf{v}_h|_K \in (\mathbb{P}_p(K))^3\},$$

$$\mathbf{\Sigma}_h = \{\underline{\underline{\sigma}}_h \in \left(L^2(\Omega)\right)^6 | \forall K \in \mathcal{T}_h, \underline{\underline{\sigma}}_h|_K \in (\mathbb{P}_p(K))^6\},$$

where $L^2(\Omega)$ is the space of square integrable functions on the domain Ω.

3 Discontinuous Galerkin method

3.1 DG formulations

3.1.1 Principles

We decide to work with the vectorial equation (2.5) of the elastodynamics system in order to establish the DG formulations considered in this study. Moreover, we choose to make a classic approximation of coefficients ρ, λ and μ considering them as piecewise-constant, i.e. constant over an element. Matrices $\mathbf{A}_x, \mathbf{A}_y$ and $\mathbf{A}_z$, depending only on these coefficients, are also piecewise-constant.

The DG method seeks an approximate solution $\mathbf{W}_h = \left(\mathbf{v}_h, \underline{\underline{\sigma}}_h\right)^T$ in the space $\mathbf{V}_h \times \mathbf{\Sigma}_h$ satisfying for all K in $\mathcal{T}_h$

$$\int_K i\omega \mathbf{W}_h \Phi + \int_K \mathbf{A}_x \frac{\partial \mathbf{W}_h}{\partial x} \Phi + \int_K \mathbf{A}_y \frac{\partial \mathbf{W}_h}{\partial y} \Phi + \int_K \mathbf{A}_z \frac{\partial \mathbf{W}_h}{\partial z} \Phi = 0,$$

where $\Phi \in V_h$. An integration by parts yields

$$\begin{aligned}\int_K i\omega \mathbf{W}_h\Phi - \int_K \mathbf{A}_x\mathbf{W}_h\frac{\partial\Phi}{\partial x} + \int_{\partial K}\mathbf{A}_x\mathbf{W}_h\Phi n_x - \int_K \mathbf{A}_y\mathbf{W}_h\frac{\partial\Phi}{\partial y} + \int_{\partial K}\mathbf{A}_y\mathbf{W}_h\Phi n_y \\ - \int_K \mathbf{A}_z\mathbf{W}_h\frac{\partial\Phi}{\partial z} + \int_{\partial K}\mathbf{A}_z\mathbf{W}_h\Phi n_z = 0.\end{aligned} \tag{3.1}$$

Defining matrix $\mathbf{D_n}$ such as

$$\begin{aligned}\mathbf{D_n} &= n_x\mathbf{A}_x + n_y\mathbf{A}_y + n_z\mathbf{A}_z \\ &= -\begin{pmatrix} 0 & 0 & 0 & \frac{n_x}{\rho} & 0 & 0 & \frac{n_y}{\rho} & 0 & \frac{n_z}{\rho} \\ 0 & 0 & 0 & 0 & \frac{n_y}{\rho} & 0 & \frac{n_x}{\rho} & \frac{n_z}{\rho} & 0 \\ 0 & 0 & 0 & 0 & 0 & \frac{n_z}{\rho} & 0 & \frac{n_y}{\rho} & \frac{n_x}{\rho} \\ n_x(\lambda+2\mu) & n_y\lambda & n_z\lambda & 0 & 0 & 0 & 0 & 0 & 0 \\ n_x\lambda & n_y(\lambda+2\mu) & n_z\lambda & 0 & 0 & 0 & 0 & 0 & 0 \\ n_x\lambda & n_y\lambda & n_z(\lambda+2\mu) & 0 & 0 & 0 & 0 & 0 & 0 \\ n_y\mu & n_x\mu & 0 & 0 & 0 & 0 & 0 & 0 & 0 \\ 0 & n_z\mu & n_y\mu & 0 & 0 & 0 & 0 & 0 & 0 \\ n_z\mu & 0 & n_x\mu & 0 & 0 & 0 & 0 & 0 & 0 \end{pmatrix} \\ &= \mathbf{Dn}, \quad \text{with } \mathbf{D} = (\mathbf{A}_x, \mathbf{A}_y, \mathbf{A}_z).\end{aligned}$$

We rewrite (3.1) as

$$\int_K i\omega \mathbf{W}_h\Phi - \int_K \mathbf{A}_x\mathbf{W}_h\frac{\partial\Phi}{\partial x} - \int_K \mathbf{A}_y\mathbf{W}_h\frac{\partial\Phi}{\partial y} - \int_K \mathbf{A}_z\mathbf{W}_h\frac{\partial\Phi}{\partial z} + \int_{\partial K}(\mathbf{D_n}\mathbf{W}_h)\,|_{\partial K}\Phi = 0. \tag{3.2}$$

We note that the term $(\mathbf{D_n}\mathbf{W}_h)\,|_{\partial K}$ will require a special treatment since $\mathbf{W}_h$ is discontinuous at an element boundary and $\mathbf{D_n}$ is constant on an element. This will be detailed later. By summing equations (3.2) over all elements, we obtain the following global equation

$$\begin{aligned}\sum_{K\in\mathcal{T}_h}\int_K i\omega \mathbf{W}_h\Phi - \sum_{K\in\mathcal{T}_h}\int_K \mathbf{A}_x\mathbf{W}_h\frac{\partial\Phi}{\partial x} - \sum_{K\in\mathcal{T}_h}\int_K \mathbf{A}_y\mathbf{W}_h\frac{\partial\Phi}{\partial y} - \sum_{K\in\mathcal{T}_h}\int_K \mathbf{A}_z\mathbf{W}_h\frac{\partial\Phi}{\partial z} \\ + \sum_{F\in\mathcal{F}_i}\int_F\left(\mathbf{D}^K_{\mathbf{n}}\mathbf{W}^K_h + \mathbf{D}^{K'}_{\mathbf{n}'}\mathbf{W}^{K'}_h\right)\Phi \\ + \sum_{F\in\mathcal{F}_b}\int_F \mathbf{D}^K_{\mathbf{n}}\mathbf{W}^K_h\Phi = 0.\end{aligned} \tag{3.3}$$

We choose to define the jump of $\mathbf{D_n}\mathbf{W}_h$ through a face F such as

$$[\![\mathbf{D_n}\mathbf{W}_h]\!] = \mathbf{D}^K_{\mathbf{n}}\mathbf{W}^K_h + \mathbf{D}^{K'}_{\mathbf{n}'}\mathbf{W}^{K'}_h \qquad \text{for } F\in\mathcal{F}_i,$$

$$[\![\mathbf{D_n}\mathbf{W}_h]\!] = \mathbf{D}^K_{\mathbf{n}}\mathbf{W}^K_h \qquad \text{for } F\in\mathcal{F}_b.$$

Finally the global DG formulation is given by

$$\begin{aligned}\sum_{K\in\mathcal{T}_h}\int_K i\omega \mathbf{W}_h\Phi - \sum_{K\in\mathcal{T}_h}\int_K \mathbf{A}_x\mathbf{W}_h\frac{\partial\Phi}{\partial x} - \sum_{K\in\mathcal{T}_h}\int_K \mathbf{A}_y\mathbf{W}_h\frac{\partial\Phi}{\partial y} - \sum_{K\in\mathcal{T}_h}\int_K \mathbf{A}_z\mathbf{W}_h\frac{\partial\Phi}{\partial z} \\ + \sum_{F\in\mathcal{F}_h}\int_F [\![\mathbf{D_n}\mathbf{W}_h\Phi]\!] = 0.\end{aligned} \tag{3.4}$$

If the support of the basis function Φ is the element K, the global formulation (3.4) reduces to a local formulation on element K. The surface integral over K's boundary is written like the sum over all K faces

$$\int_{\partial K} \mathbf{D_n} \mathbf{W}_h \Phi = \sum_{F \in \mathcal{F}(K)} \int_F \mathbf{D_n} \mathbf{W}_h \Phi.$$

Moreover as matrices $\mathbf{A}_x, \mathbf{A}_y$ and $\mathbf{A}_z$ are piecewise-constant, we obtain the following local equation

$$\begin{aligned}\int_K i\omega \mathbf{W}_h^K \Phi^K - \int_K \mathbf{A}_x^K \mathbf{W}_h^K \frac{\partial \Phi^K}{\partial x} - \int_K \mathbf{A}_y^K \mathbf{W}_h^K \frac{\partial \Phi^K}{\partial y} - \int_K \mathbf{A}_z^K \mathbf{W}_h^K \frac{\partial \Phi^K}{\partial z} \\ + \sum_{F \in \mathcal{F}(K)} \int_F \left(\mathbf{D_n} \mathbf{W}_h\right)|_F \Phi^K = 0.\end{aligned} \tag{3.5}$$

To compute the numerical trace $\left(\mathbf{D_n} \mathbf{W}_h\right)|_F$ in equation (3.5), we consider two options: a centered scheme and an upwind scheme.

3.1.2 Centered flux DG scheme

To establish the centered flux DG formulation, we approximate $\left(\mathbf{D_n} \mathbf{W}_h\right)|_F$ on a face F by its average, i.e

$$\left(\mathbf{D_n} \mathbf{W}_h\right)|_F = \left\{\mathbf{D_n} \mathbf{W}_h\right\}.$$

Using this definition, the local equation (3.5) becomes

$$\begin{aligned}\int_K i\omega \mathbf{W}_h^K \Phi^K - \int_K \mathbf{A}_x^K \mathbf{W}_h^K \frac{\partial \Phi^K}{\partial x} - \int_K \mathbf{A}_y^K \mathbf{W}_h^K \frac{\partial \Phi^K}{\partial y} - \int_K \mathbf{A}_z^K \mathbf{W}_h^K \frac{\partial \Phi^K}{\partial z} \\ + \sum_{F \in \partial K \cap \partial K'} \int_F \frac{1}{2} \left(\mathbf{D}_{\mathbf{n}}^K \mathbf{W}_h^K + \mathbf{D}_{\mathbf{n}'}^{K'} \mathbf{W}_h^{K'}\right) \Phi^K \\ + \sum_{F \in \partial K \cap \partial \Omega} \int_F \mathbf{D}_{\mathbf{n}}^K \mathbf{W}_h^K \Phi^K = 0.\end{aligned} \tag{3.6}$$

We verify that summing the centered flux local equation over all the elements yields the expected global DG equation

$$\begin{aligned}\sum_{K \in \mathcal{T}_h} \int_K i\omega \mathbf{W}_h^K \Phi^K - \sum_{K \in \mathcal{T}_h} \int_K \mathbf{A}_x^K \mathbf{W}_h^K \frac{\partial \Phi^K}{\partial x} - \sum_{K \in \mathcal{T}_h} \int_K \mathbf{A}_y^K \mathbf{W}_h^K \frac{\partial \Phi^K}{\partial y} - \sum_{K \in \mathcal{T}_h} \int_K \mathbf{A}_z^K \mathbf{W}_h^K \frac{\partial \Phi^K}{\partial z} \\ + \sum_{F \in \mathcal{F}_h} \int_F \{\mathbf{D_n} \mathbf{W}_h\} [\![\Phi]\!] = 0.\end{aligned}$$

Let us now recall the property linking the average and the jump

$$[\![\mathbf{uv}]\!] = \{\mathbf{u}\}[\![\mathbf{v}]\!] + [\![\mathbf{u}]\!]\{\mathbf{v}\},$$

and the fact that if $\mathbf{W}_h$ is solution of the elastodynamics equations (2.1) then,$[\![\mathbf{W}_h]\!] = 0$. Thus, if we multiply $\mathbf{W}_h$ by a constant matrix $\mathbf{D_n}$, we have $[\![\mathbf{D_n} \mathbf{W}_h]\!] = 0$, and we can deduce that

$$\int_{\mathcal{F}_h} \{\mathbf{D_n} \mathbf{W}_h\}[\![\Phi]\!] = \sum_{F \in \mathcal{F}_h} \int_F \{\mathbf{D_n} \mathbf{W}_h\}[\![\Phi]\!] + \sum_{F \in \mathcal{F}_h} \int_F [\![\mathbf{D_n} \mathbf{W}_h]\!]\{\Phi\} = \int_{\mathcal{F}_h} [\![\mathbf{D_n} \mathbf{W}_h \Phi]\!].$$

Replacing the surface integral we recover the global equation (3.4).

In equation (3.6), we decompose each component of the vector $\mathbf{W}_h^K$ in the basis $\Phi^K = \left(\varphi^K\right)_i$

$$\mathbf{W}_h^K = \sum_{j=1}^{d_i} \mathbf{W}_j^K \varphi_j^K, \tag{3.7}$$

where

$$\mathbf{W}_j^K = \left(v_{x_j}, v_{y_j}, v_{z_j}, \sigma_{xx_j}, \sigma_{xx_j}, \sigma_{yy_j}, \sigma_{zz_j}, \sigma_{xy_j}, \sigma_{yz_j}, \sigma_{xz_j}\right)^T.$$

Choosing the test function as $\varphi_l^K \in \Phi^K$, $l = 1, d_i$, we obtain the following local discretization

$$\begin{aligned} i\omega \sum_{j=1}^{d_i} \mathbf{W}_j^K \int_K \varphi_j^K \varphi_l^K - \mathbf{A}_x^K \sum_{j=1}^{d_i} \mathbf{W}_j^K \int_K \varphi_j^K \frac{\partial \varphi_l^K}{\partial x} & \\ - \mathbf{A}_y^K \sum_{j=1}^{d_i} \mathbf{W}_j^K \int_K \varphi_j^K \frac{\partial \varphi_l^K}{\partial y} & \\ - \mathbf{A}_z^K \sum_{j=1}^{d_i} \mathbf{W}_j^K \int_K \varphi_j^K \frac{\partial \varphi_l^K}{\partial z} & \\ + \sum_{F \in \partial K \cap \partial K'} \frac{1}{2} \left(\mathbf{D}_{\mathbf{n}}^K \sum_{j=1}^{d_i} \mathbf{W}_j^K \int_F \varphi_j^K \varphi_l^K + \mathbf{D}_{\mathbf{n}}^{K'} \sum_{j=1}^{d_i} \mathbf{W}_j^{K'} \int_F \varphi_j^{K'} \varphi_l^K \right) & \\ + \sum_{F \in \partial K \cap \partial \Omega} \int_F \mathbf{D}_{\mathbf{n}}^K \mathbf{W}_h^K \varphi_l^K = 0. & \end{aligned} \tag{3.8}$$

Finally we write the above equation in a matrix form

$$\begin{aligned} i\omega \mathcal{M}^K \underline{\mathbf{W}}^K - \mathbf{A}_x^K \mathcal{D}_x^K \underline{\mathbf{W}}^K - \mathbf{A}_y^K \mathcal{D}_y^K \underline{\mathbf{W}}^K - \mathbf{A}_z^K \mathcal{D}_z^K \underline{\mathbf{W}}^K & \\ + \sum_{F \in \partial K \cap \partial K'} \frac{1}{2} \left(\mathbf{D}_{\mathbf{n}}^K \mathcal{E}_1^K \underline{\mathbf{W}}^K + \mathbf{D}_{\mathbf{n}}^{K'} \mathcal{E}_2^K \underline{\mathbf{W}}^{K'} \right) & \\ + \sum_{F \in \partial K \cap \partial \Omega} \int_F \mathbf{D}_{\mathbf{n}}^K \mathbf{W}_h^K \Phi^K = 0, & \end{aligned} \tag{3.9}$$

where

$$\begin{aligned} \underline{\mathbf{W}}^K &= \left(\mathbf{W}_1^K, ..., \mathbf{W}_{d_i}^K\right)^T, \\ \mathcal{M}^K(i,j) &= \int_K \varphi_j^K \varphi_i^K, \\ \mathcal{D}_u^K(i,j) &= \int_K \varphi_j^K \frac{\partial \varphi_i^K}{\partial u}, \text{ with } u = x, y, z, \\ \mathcal{E}_1^K(i,j) &= \int_F \varphi_j^K \varphi_i^K, \\ \mathcal{E}_2^K(i,j) &= \int_F \varphi_j^{K'} \varphi_i^K. \end{aligned} \tag{3.10}$$

We note that we have not developed the boundary integral $\displaystyle\sum_{F\in\partial K\cap\partial\Omega}\int_F \mathbf{D}_{\mathbf{n}}^K \mathbf{W}_h^K \Phi^K$. We will detail the treatment of this term in section 3.1.4.

By summing the local equation (3.9) over all elements, the global equation (3.4) can be written as

$$\begin{aligned} i\omega \sum_{K\in\mathcal{T}_h} \mathcal{M}^K \underline{\mathbf{W}}^K - \sum_{K\in\mathcal{T}_h} \mathbf{A}_x^K \mathcal{D}_x^K \underline{\mathbf{W}}^K - \sum_{K\in\mathcal{T}_h} \mathbf{A}_y^K \mathcal{D}_y^K \underline{\mathbf{W}}^K - \sum_{K\in\mathcal{T}_h} \mathbf{A}_z^K \mathcal{D}_z^K \underline{\mathbf{W}}^K \\ + \sum_{K\in\mathcal{T}_h} \sum_{F\in\partial K\cap\partial K'} \frac{1}{2}\left(\mathbf{D}_{\mathbf{n}}^K \mathcal{E}_1^K \underline{\mathbf{W}}^K + \mathbf{D}_{\mathbf{n}}^{K'} \mathcal{E}_2^K \underline{\mathbf{W}}^{K'}\right) \\ + \sum_{K\in\mathcal{T}_h} \sum_{F\in\partial K\cap\partial\Omega} \int_F \mathbf{D}_{\mathbf{n}}^K \mathbf{W}_h^K \Phi^K = 0. \end{aligned} \tag{3.11}$$

3.1.3 Upwind flux DG scheme

Before developing the upwind flux DG formulation, we need to look at the some properties of the matrix $\mathbf{D}_{\mathbf{n}}$. It can be shown that $\mathbf{D}_{\mathbf{n}}$ is a square matrix that can be diagonalized. The corresponding eigenvalues are

$$\xi_1 = -v_p,\ \xi_2 = \xi_3 = -v_s,\ \xi_4 = \xi_5 = \xi_6 = 0,\ \xi_7 = \xi_8 = v_s,\ \xi_9 = v_p,$$

where $v_p = \sqrt{\dfrac{\lambda + 2\mu}{\rho}}$ and $v_s = \sqrt{\dfrac{\mu}{\rho}}$. The associated eigenvectors are gathered in 9 × 9 matrix $\mathbf{R}_{\mathbf{n}}$, where kth column is the eigenvector associated of the eigenvalue ξ_k

$$\mathbf{R}_{\mathbf{n}} = \begin{pmatrix} n_x\, v_p & n_z\, v_s & 0 & 0 & 0 & 0 & \cdots \\ n_y\, v_p & 0 & n_z\, v_s & 0 & 0 & 0 & \cdots \\ n_z\, v_p & -n_x\, v_s & -n_y\, v_s & 0 & 0 & 0 & \cdots \\ \lambda + 2\,\mu\, n_x^2 & 2\,\mu\, n_x\, n_z & 0 & 2\, n_y\, n_z & 0 & 0 & \cdots \\ \lambda + 2\,\mu\, n_y^2 & 0 & 2\,\mu\, n_y\, n_z & 0 & 2\, n_x\, n_z & 0 & \cdots \\ 2\,\mu\, n_z^2 + \lambda & -2\,\mu\, n_x\, n_z & -2\,\mu\, n_y\, n_z & 0 & 0 & 2\, n_x\, n_y & \cdots \\ 2\,\mu\, n_y\, n_x & \mu\, n_y\, n_z & \mu\, n_x\, n_z & -n_x\, n_z & -n_y\, n_z & n_z^2 & \cdots \\ 2\,\mu\, n_y\, n_z & -\mu\, n_x\, n_y & \mu\,\left(n_z^2 - n_y^2\right) & n_x^2 & -n_y\, n_x & -n_z\, n_x & \cdots \\ 2\,\mu\, n_z\, n_x & \mu\,\left(n_z^2 - n_x^2\right) & -\mu\, n_x\, n_y & -n_x\, n_y & {n_y}^2 & -n_z\, n_y & \cdots \end{pmatrix},$$

$$\begin{pmatrix} \cdots & 0 & -n_z\, v_s & -n_x\, v_p \\ \cdots & -n_z\, v_s & 0 & -n_y\, v_p \\ \cdots & n_y\, v_s & n_x\, v_s & -n_z\, v_p \\ \cdots & 0 & 2\,\mu\, n_x\, n_z & \lambda + 2\,\mu\, n_x^2 \\ \cdots & 2\,\mu\, n_y\, n_z & 0 & \lambda + 2\,\mu\, n_y^2 \\ \cdots & -2\,\mu\, n_y\, n_z & -2\,\mu\, n_x\, n_z & 2\,\mu\, n_z^2 + \lambda \\ \cdots & \mu\, n_x\, n_z & \mu\, n_y\, n_z & 2\,\mu\, n_y\, n_x \\ \cdots & \mu\,\left(n_z^2 - n_y^2\right) & -\mu\, n_x\, n_y & 2\,\mu\, n_y\, n_z \\ \cdots & -\mu\, n_x\, n_y & \mu\,\left(n_z^2 - n_x^2\right) & 2\,\mu\, n_z\, n_x \end{pmatrix}.$$

We define $\mathbf{D}_{\mathbf{n}}^+$ such as

$$\mathbf{D}_{\mathbf{n}}^+ = \mathbf{R}_{\mathbf{n}} \mathbf{\Lambda}^+ \left(\mathbf{R}_{\mathbf{n}}\right)^{-1},$$

and $\mathbf{D}_{\mathbf{n}}^-$ such as

$$\mathbf{D}_{\mathbf{n}}^- = \mathbf{R}_{\mathbf{n}} \mathbf{\Lambda}^- \left(\mathbf{R}_{\mathbf{n}}\right)^{-1},$$

where $\mathbf{\Lambda}^+$ is the diagonal matrix built with the positive eigenvalues of $\mathbf{D_n}$ and $\mathbf{\Lambda}^-$ the one including negative eigenvalues of $\mathbf{D_n}$; $\mathbf{R_n}$ is the matrix defined above. We remark that we have

$$\mathbf{D_n} = \mathbf{D_n^+} + \mathbf{D_n^-} \quad \text{and} \quad |\mathbf{D_n}| = \mathbf{D_n^+} - \mathbf{D_n^-}. \tag{3.12}$$

We remind the local equation (3.5) of the DG formulation

$$\begin{aligned}\int_K i\omega \mathbf{W}_h^K \Phi^K - \int_K \mathbf{A}_x^K \mathbf{W}_h^K \frac{\partial \Phi^K}{\partial x} - \int_K \mathbf{A}_y^K \mathbf{W}_h^K \frac{\partial \Phi^K}{\partial y} - \int_K \mathbf{A}_z^K \mathbf{W}_h^K \frac{\partial \Phi^K}{\partial z} \\ + \sum_{F\in\mathcal{F}(K)} \int_F \left(\mathbf{D_n}\mathbf{W}_h\right)|_F \Phi^K = 0.\end{aligned}$$

For the upwind flux DG formulation, we define the numerical trace $\left(\mathbf{D_n}\mathbf{W}_h\right)|_F$ of $\mathbf{D_n}\mathbf{W}$ on a face F as

$$\left(\mathbf{D_n}\mathbf{W}_h\right)|_F = \left(\mathbf{D_n^{\mathit{K}}}\right)^+ \mathbf{W}_h^K + \left(\mathbf{D_n^{\mathit{K'}}}\right)^- \mathbf{W}_h^{K'}. \tag{3.13}$$

By replacing in equation (3.5) the surface term by its approximation for an interior face, we obtain

$$\begin{aligned}\int_K i\omega \mathbf{W}_h^K \Phi^K - \int_K \mathbf{A}_x^K \mathbf{W}_h^K \frac{\partial \Phi^K}{\partial x} - \int_K \mathbf{A}_y^K \mathbf{W}_h^K \frac{\partial \Phi^K}{\partial y} - \int_K \mathbf{A}_z^K \mathbf{W}_h^K \frac{\partial \Phi^K}{\partial z} \\ + \sum_{F\in\partial K\cap\partial K'} \int_F \left[\left(\mathbf{D_n^{\mathit{K}}}\right)^+ \mathbf{W}_h^K + \left(\mathbf{D_n^{\mathit{K'}}}\right)^- \mathbf{W}_h^{K'}\right] \Phi^K \\ + \sum_{F\in\partial K\cap\partial\Omega} \int_F \mathbf{D_n^{\mathit{K}}} \mathbf{W}_h^K \Phi^K = 0.\end{aligned}$$

Using the decomposition (3.7) of $\mathbf{W}^K$ in the basis Φ^K and taking $\varphi_l^K, l = 1, d_i$ as test-function, we obtain the local equation for the upwind DG schema

$$\begin{aligned}i\omega \sum_{j=1}^{d_i} \mathbf{W}_j^K \int_K \varphi_j^K \varphi_l^K - \mathbf{A}_x^K \sum_{j=1}^{d_i} \mathbf{W}_j^K \int_K \varphi_j^K \frac{\partial \varphi_l^K}{\partial x} \\ - \mathbf{A}_y^K \sum_{j=1}^{d_i} \mathbf{W}_j^K \int_K \varphi_j^K \frac{\partial \varphi_l^K}{\partial y} \\ - \mathbf{A}_z^K \sum_{j=1}^{d_i} \mathbf{W}_j^K \int_K \varphi_j^K \frac{\partial \varphi_l^K}{\partial z} \\ + \sum_{F\in\partial K\cap\partial K'} \left(\left(\mathbf{D_n^{\mathit{K}}}\right)^+ \sum_{j=1}^{d_i} \mathbf{W}_j^K \int_F \varphi_j^K \varphi_l^K + \left(\mathbf{D_n^{\mathit{K'}}}\right)^- \sum_{j=1}^{d_i} \mathbf{W}_j^{K'} \int_F \varphi_j^{K'} \varphi_l^K \right) \\ + \sum_{F\in\partial K\cap\partial\Omega} \int_F \mathbf{D_n^{\mathit{K}}} \mathbf{W}_h^K \varphi_l^K = 0.\end{aligned} \tag{3.14}$$

Similarly to the centered scheme, we write the above equation in a matrix form

$$\begin{aligned} i\omega \mathcal{M}^K \underline{\mathbf{W}}^K &- \mathbf{A}_x^K \mathcal{D}_x^K \underline{\mathbf{W}}^K - \mathbf{A}_y^K \mathcal{D}_y^K \underline{\mathbf{W}}^K - \mathbf{A}_z^K \mathcal{D}_z^K \underline{\mathbf{W}}^K \\ &+ \sum_{F\in\partial K\cap\partial K'} \left(\left(\mathbf{D}_{\mathbf{n}}^K\right)^+ \mathcal{E}_1^K \underline{\mathbf{W}}^K + \left(\mathbf{D}_{\mathbf{n}}^{K'}\right)^- \mathcal{E}_2^K \underline{\mathbf{W}}^{K'} \right) \\ &+ \sum_{F\in\partial K\cap\partial\Omega} \int_F \mathbf{D}_{\mathbf{n}}^K \mathbf{W}_h^K \Phi^K = 0, \end{aligned} \tag{3.15}$$

where matrices $\mathcal{M}^K, \mathcal{D}_u^K, u = x, y, z, \mathcal{E}_1^K$ and $\mathcal{E}_2^K$ are defined by (3.10). Finally the global equation for the upwind DG scheme in a matrix form is

$$\begin{aligned} i\omega \sum_{K\in\mathcal{T}_h} \mathcal{M}^K \underline{\mathbf{W}}^K &- \sum_{K\in\mathcal{T}_h} \mathbf{A}_x^K \mathcal{D}_x^K \underline{\mathbf{W}}^K - \sum_{K\in\mathcal{T}_h} \mathbf{A}_y^K \mathcal{D}_y^K \underline{\mathbf{W}}^K - \sum_{K\in\mathcal{T}_h} \mathbf{A}_z^K \mathcal{D}_z^K \underline{\mathbf{W}}^K \\ &+ \sum_{K\in\mathcal{T}_h} \sum_{F\in\partial K\cap\partial K'} \left(\left(\mathbf{D}_{\mathbf{n}}^K\right)^+ \mathcal{E}_1^K \underline{\mathbf{W}}^K + \left(\mathbf{D}_{\mathbf{n}}^{K'}\right)^- \mathcal{E}_2^K \underline{\mathbf{W}}^{K'} \right) \\ &+ \sum_{K\in\mathcal{T}_h} \sum_{F\in\partial K\cap\partial\Omega} \int_F \mathbf{D}_{\mathbf{n}} \mathbf{W} \varphi = 0. \end{aligned} \tag{3.16}$$

3.1.4 Boundary conditions

We are concerned here with the numerical treatment of the integral term over the boundary of the computational domain,

$$\sum_{F\in\partial K\cap\partial\Omega} \int_F \mathbf{D}_{\mathbf{n}} \mathbf{W} \varphi.$$

Two boundary conditions have been introduced in the problem statement in section 2.1

- Free surface condition to simulate a physical interface between the domain and the air
- Absorbing boundary condition to simulate an infinite domain

Absorbing boundary condition. The objective is to define an appropriate numerical treatment when the theoretically unbounded propagation domain is artificially truncated. More precisely, we would like impose some conditions on the corresponding boundary faces which allow the absorption of the waves when they reach the artificial boundary. There exist several possible strategies including Perfectly Matched Layers (PML, C-PML, etc.) absorbing conditions which are approximations of an exact transparent condition. The latter option has be adopted in this study. By using the plus-minus decomposition of the flux matrix (3.12), we can define a simple treatment which consists in considering that the inflow flux is zero for each face on the artificial boundary, i.e.

$$\left(\mathbf{D}_{\mathbf{n}}\right)^- \mathbf{W} = 0 \text{ on } \mathcal{F}_b. \tag{3.17}$$

Then

$$\begin{aligned} \int_{F_b} \mathbf{D}_{\mathbf{n}} \mathbf{W}_h \varphi &\simeq \int_{F_b} \left(\mathbf{D}_{\mathbf{n}}^K\right)^+ \mathbf{W}_h^K \varphi \\ &\simeq \left(\mathbf{D}_{\mathbf{n}}^K\right)^+ \sum_{j=1}^{d_i} \mathbf{W}_j^K \int_{F_b} \varphi_j^K \varphi. \end{aligned}$$

Setting $\varphi = \varphi_i^K$ we have

$$\int_{F_b} \left(\mathbf{D}_{\mathbf{n}}^K\right)^+ \mathbf{W}_h^K \varphi_i^K = \left(\mathbf{D}_{\mathbf{n}}^K\right)^+ \underline{\mathbf{W}}^K \mathcal{B}^K,$$

where $\mathcal{B}^K(i,j) = \displaystyle\int_{F_b} \varphi_j^K \varphi_i^K$.

Free surface condition. On a free surface boundary we impose

$$\underline{\underline{\sigma}}\mathbf{n} = 0, \tag{3.18}$$

and no particular condition is applied to the velocity components. We then have

$$\int_{F_b} \mathbf{D}_{\mathbf{n}}^K \mathbf{W}_h^K \varphi = \int_{F_b} \mathbf{D}_{\mathbf{n}}^K \mathbf{L} \mathbf{W}_h^K \varphi,$$

where $\mathbf{L} = \begin{pmatrix} 1 & 0 & 0 & 0 & 0 & 0 & 0 & 0 & 0 \\ 0 & 1 & 0 & 0 & 0 & 0 & 0 & 0 & 0 \\ 0 & 0 & 1 & 0 & 0 & 0 & 0 & 0 & 0 \\ 0 & 0 & 0 & 0 & 0 & 0 & 0 & 0 & 0 \\ 0 & 0 & 0 & 0 & 0 & 0 & 0 & 0 & 0 \\ 0 & 0 & 0 & 0 & 0 & 0 & 0 & 0 & 0 \\ 0 & 0 & 0 & 0 & 0 & 0 & 0 & 0 & 0 \\ 0 & 0 & 0 & 0 & 0 & 0 & 0 & 0 & 0 \\ 0 & 0 & 0 & 0 & 0 & 0 & 0 & 0 & 0 \end{pmatrix}$.

Using $\varphi = \varphi_i^K$ the numerical flux on free surface boundary is

$$\int_{F_b} \mathbf{D}_{\mathbf{n}}^K \mathbf{L} \mathbf{W}_h^K \varphi_i^K = \mathbf{D}_{\mathbf{n}}^K \mathbf{L} \underline{\mathbf{W}}^K \mathcal{B}^K.$$

Finally, the global discrete system writes

$$\begin{aligned} i\omega \sum_{K\in\mathcal{T}_h} \mathcal{M}^K \underline{\mathbf{W}}^K - \sum_{K\in\mathcal{T}_h} \mathbf{A}_x^K \mathcal{D}_x^K \underline{\mathbf{W}}^K - \sum_{K\in\mathcal{T}_h} \mathbf{A}_y^K \mathcal{D}_y^K \underline{\mathbf{W}}^K - \sum_{K\in\mathcal{T}_h} \mathbf{A}_z^K \mathcal{D}_z^K \underline{\mathbf{W}}^K & \\ + \sum_{K\in\mathcal{T}_h} \sum_{F\in\partial K\cap\partial K'} \left(\mathbf{H}_{\mathbf{n}}^K \mathcal{E}_1^K \underline{\mathbf{W}}^K + \mathbf{H}_{\mathbf{n}}^{K'} \mathcal{E}_2^K \underline{\mathbf{W}}^{K'} \right) & \\ + \sum_{K\in\mathcal{T}_h} \sum_{F\in\partial K\cap\partial\Omega} \mathbf{G}_{\mathbf{n}} \mathcal{B}^K \underline{\mathbf{W}}^K = 0, & \end{aligned} \tag{3.19}$$

where $\mathbf{H}_{\mathbf{n}}^K = \left(\mathbf{D}_{\mathbf{n}}^K\right)^+$ and $\mathbf{H}_{\mathbf{n}}^{K'} = \left(\mathbf{D}_{\mathbf{n}}^{K'}\right)^-$ in the case of the upwind numerical flux, $\mathbf{H}_{\mathbf{n}}^K = \frac{1}{2}\mathbf{D}_{\mathbf{n}}^K$ and $\mathbf{H}_{\mathbf{n}}^{K'} = \frac{1}{2}\mathbf{D}_{\mathbf{n}}^{K'}$ for the centered numerical scheme, and $\mathbf{G}_{\mathbf{n}} = \mathbf{D}_{\mathbf{n}}^K \mathbf{L}$ or $\mathbf{G}_{\mathbf{n}} = \left(\mathbf{D}_{\mathbf{n}}^K\right)^+$ depending on the type of boundary conditions.

4 Two-dimensional numerical results

In this section, we provide some numerical results in 2D to assess the performances (accuracy and efficiency) of the centered and upwind DG schemes introduced in the previous section. These schemes have been implemented in a Fortran 90 software. We use the MUMPS sparse direct solver for the resolution of the linear system (see [7] for more details) resulting from the DG discretization scheme.

Numerical experiments are performed on a hardware system equipped with 2 quad-core Nehalem Intel® Xeon® X5550/2,66 GHz CPUs and 24Go (DDR3 1333 MHz) of RAM.

Two simple problems, the propagation of a plane wave in a homogeneous medium and the scattering of a plane wave by a disk, and one heterogeneous problem, the scattering of a plane wave by a solid disk, are considered. We remind that to propagate the waves we have to solve the elastic Helmholtz equations

$$\left\{\begin{array}{lcll} i\omega\rho(\mathbf{x})\mathbf{v}(\mathbf{x}) & = & \nabla\cdot\underline{\underline{\sigma}}(\mathbf{x}) + f(\mathbf{x}) & \text{in } \Omega, \\ i\omega\underline{\underline{\sigma}}(\mathbf{x}) & = & \underline{\underline{C}}(\mathbf{x})\ \underline{\underline{\epsilon}}(\mathbf{v}(\mathbf{x})) & \text{in } \Omega, \end{array}\right. \tag{4.1}$$

4.1 Plane wave propagation in an homogeneous medium

We first consider the simple test problem of the propagation of a plane wave in an homogeneous medium. The computational domain Ω is a 10000 $m \times 10000$ m square. The physical properties of the medium are $\rho = 1000\ kg.m^{-3}$ and values of Lamé's coefficients λ and μ that are set to 8 MPa and 4 MPa respectively. These values imply a velocity v_p of P-waves equal to 4000 $m.s^{-1}$ and a velocity v_s of S-waves equal to 2000 $m.s^{-1}$. On the boundaries we impose an absorbing condition with a plane wave incident field

$$U = \nabla e^{i(k_x\cos\theta x + k_z\sin\theta z)} = \begin{pmatrix} V_{x0} \\ V_{z0} \\ \sigma_{xx0} \\ \sigma_{zz0} \\ \sigma_{xz0} \end{pmatrix} e^{i(k_x\cos\theta x + k_z\sin\theta z)},$$

where $k = \sqrt{k_x^2 + k_z^2} = \dfrac{\omega}{v_p}$ is the wavenumber, $k_x = \dfrac{\omega}{v_p}\cos\theta$ and $k_z = \dfrac{\omega}{v_p}\sin\theta$, and θ is the incidence angle. ω is the angular frequency, $\omega = 2\pi f$ where f is the frequency. If we choose arbitrarily V_{x0}, we can express the other components such as

$$\left\{\begin{array}{l} V_{z0} = \dfrac{k_x k_z\,(\lambda+\mu)}{\rho\omega^2 - k_x^2\mu - k_z^2\lambda + 2\mu)} V_{x0} \\ \sigma_{xx0} = \dfrac{-1}{\omega}\left(k_x\,(\lambda+2\mu)\,V_{x0} + \lambda k_z V_{z0}\right) \\ \sigma_{zz0} = \dfrac{-1}{\omega}\left(\lambda k_x V_{x0} + (\lambda+2\mu)\,k_z V_{z0}\right) \\ \sigma_{xz0} = \dfrac{-\mu}{\omega}\left(k_z V_{x0} + k_x V_{z0}\right). \end{array}\right.$$

In the simulations we choose θ equal to 0 and $f = 2\ Hz$, then $\omega = 4\pi \simeq 12.56\ Hz$. We discretize the computational domain Ω into three unstructured meshes with respectively 3000, 10 000 and 45 000 elements. Two of these meshes are shown on figs. 4.1 and 4.2; their characteristics are given in table 4.1.

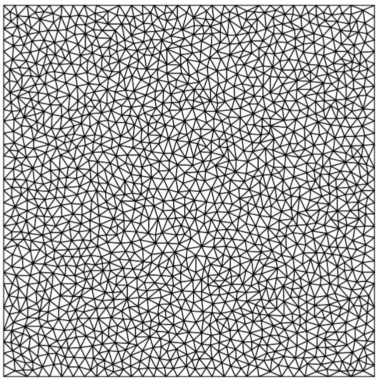

Figure 4.1: Discretization of Ω: mesh M1, 3000 elements.

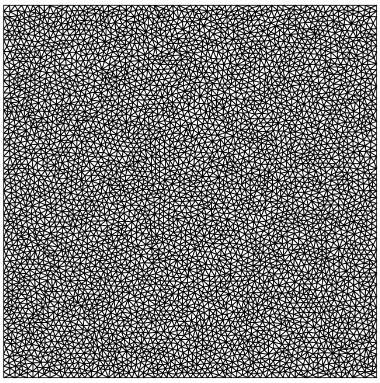

Figure 4.2: Discretization of Ω: mesh M2, 10000 elements.

Mesh	# Mesh elements	# Mesh vertices	h_{min}	h_{max}	h_{min}/h_{max}
M1	3100	1620	193.6	625.0	3.2
M2	10 300	5200	107.5	312.5	2.9
M3	45 000	22 500	45.4	156.2	3.5

Table 4.1: Characteristics of the three meshes.

We compare the obtained numerical solutions by focusing on the V_x component. When using the coarsest mesh with 3000 triangles and the DGFD-$\mathbb{P}_1$ formulation, we obtain the numerical solution shown on figs. 4.4 and 4.5 for the centered DG scheme and upwind DG scheme respectively. We can compare these two solutions to the exact one represented on fig. 4.3. Clearly, for this relatively coarse mesh, the DGFD-$\mathbb{P}_1$ based on the centered scheme solution is notably less accurate than the solution obtained with the upwind scheme. Increasing the interpolation degree (figs. 4.6 and 4.7) or the resolution of the mesh (figs. 4.8 and 4.9) lead to numerical solutions that are closer to the exact one. These results are confirmed by the 1D x-wise plots of the V_x component for $y = 5000\ m$ on figs. 4.10 to 4.12. On these plots, the solution is recorded every $10\ m$ on the $x-$axis.

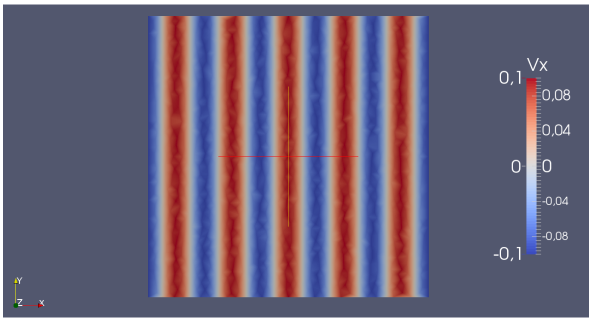

Figure 4.3: Exact solution, V_x component.

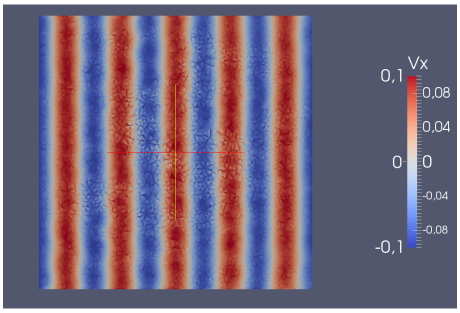

Figure 4.4: Numerical solution, mesh M1, centered flux DGFD-$\mathbb{P}_1$ cheme, V_x component.

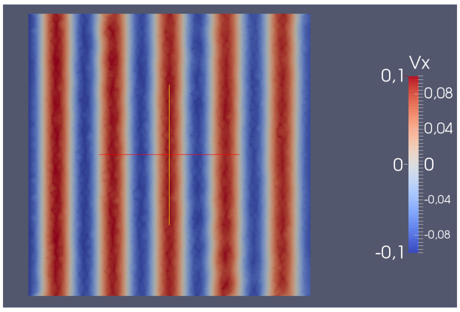

Figure 4.5: Numerical solution, mesh M1, upwind flux DGFD-$\mathbb{P}_1$ scheme, V_x component.

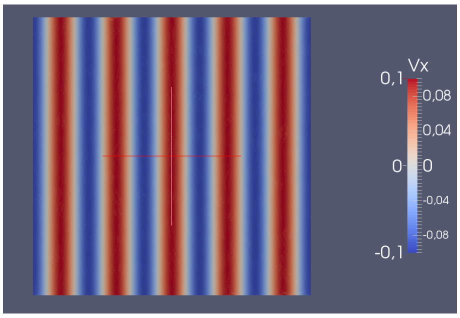

Figure 4.6: Numerical solution, mesh M1, centered flux DGFD-$\mathbb{P}_2$ scheme, V_x component.

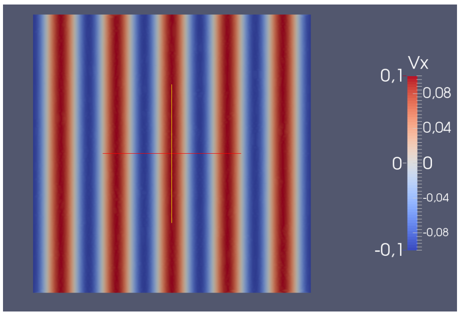

Figure 4.7: Numerical solution, mesh M1, upwind flux DGFD-$\mathbb{P}_2$ scheme, V_x component.

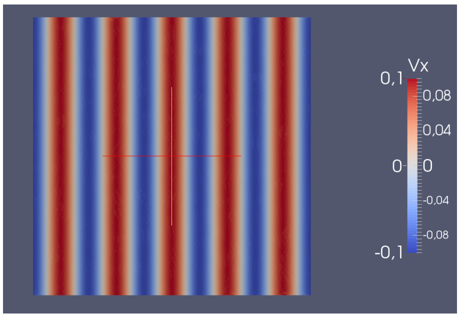

Figure 4.8: Numerical solution, mesh M2, centered flux DGFD-$\mathbb{P}_1$ scheme, V_x component.

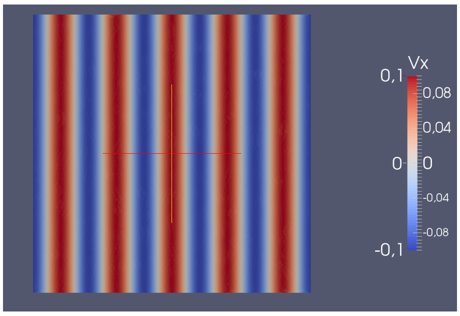

Figure 4.9: Numerical solution, mesh M2, upwind flux DGFD-$\mathbb{P}_1$ scheme, V_x component.

Fig. 4.14 shows the numerical convergence of the centered and upwind DGFD methods. These two graphs confirm that the centered DGFD scheme is less accurate than the upwind DGFD scheme and we observe that the centered DGFD scheme converges with order p whereas upwind DGFD scheme converges with order $p+1$ i.e. with optimal rate.

The computational performances of both methods for all simulations of this test problem are summarized in tables 4.2 for the number of non-zero terms in the global matrix and the memory

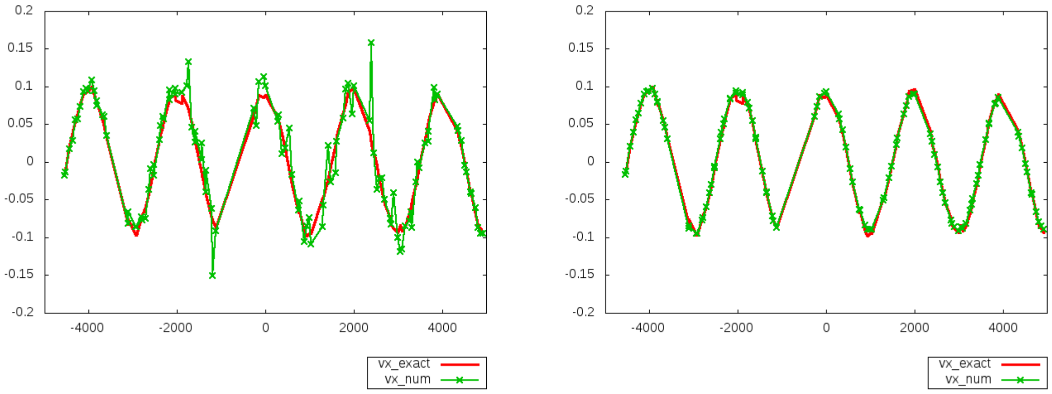

Figure 4.10: x-wise distribution of V_x, mesh M1: in red line the exact solution, in green cross the centered (left) and upwind (right) DGFD-$\mathbb{P}_1$ solution.

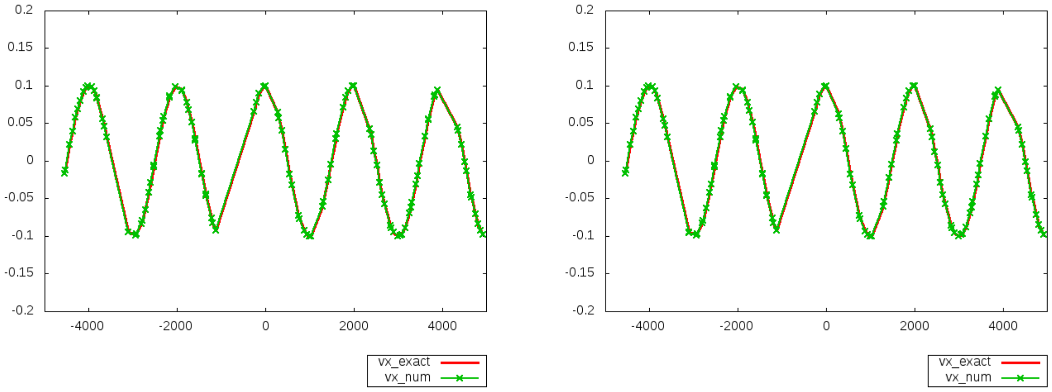

Figure 4.11: x-wise distribution of V_x, mesh M1: in red line the exact solution, in green cross the centered (left) and upwind (right) DGFD-$\mathbb{P}_2$ solution.

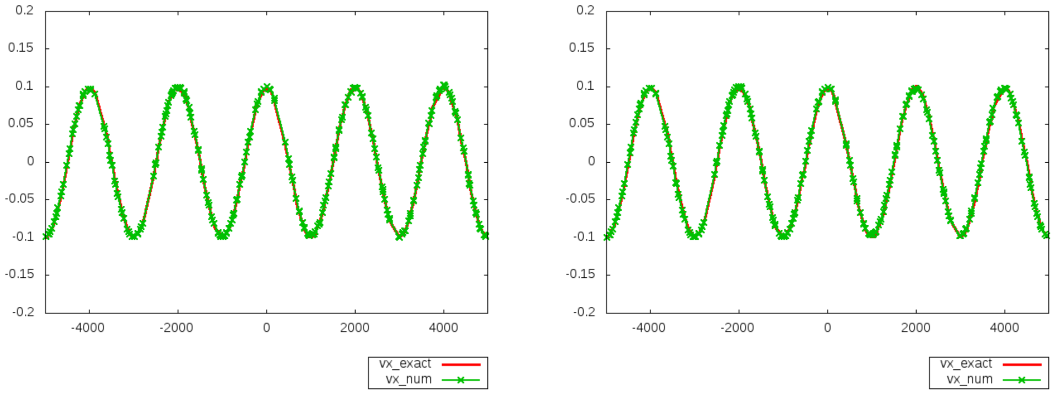

Figure 4.12: x-wise distribution of V_x, mesh M2: in red line the exact solution, in green cross the centered (left) and upwind (right) DGFD-$\mathbb{P}_1$ solution.

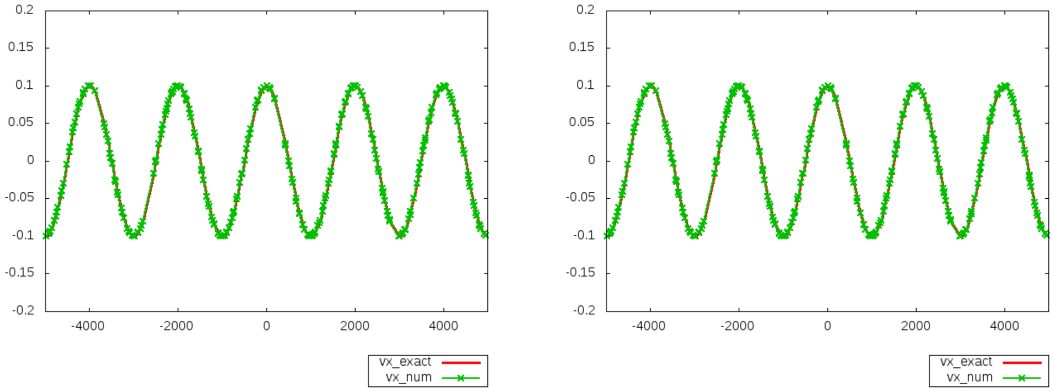

Figure 4.13: x-wise distribution of V_x, mesh M2: in red line the exact solution, in green cross the centered (left) and upwind (right) DGFD-$\mathbb{P}_1$ solution.

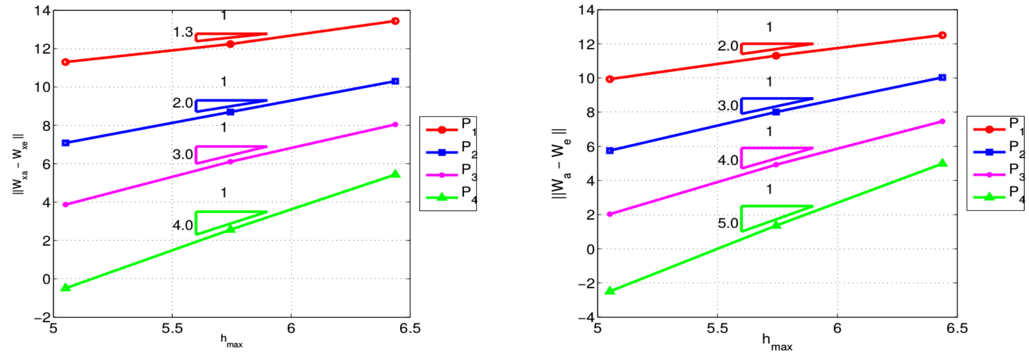

Figure 4.14: Convergence order of the centered (left) and upwind (right) flux DGFD methods for plane wave propagation in a homogeneous medium.

used (in MB), 4.3 for the time required for the construction of the global matrix (in seconds) and for the resolution (in seconds) and 4.4-4.5 for the mean and relative errors in the V_x and σ_{xx} components. The upwind DG scheme requires more memory space than the centered DG scheme. This is a result of the fact that there is more non-zero terms in the global matrix in the former case (at least 1.5 times more non-zero terms). Albeit this increase in the number of non-zero terms in the global matrix, the construction of the L and U factors for the upwind DG discrete operator does not require more CPU than that of the corresponding factors for the centered DG discrete operator. However, a difference in CPU times is clearly observed in the solution time.

# Mesh elements	Interpolation degree	Non-zeros terms		Memory (MB)	
		Cent. scheme	Upw. scheme	Cent. scheme	Upw. scheme
3100	1	7.5e+05	1.5e+06	204	288
10300	1	2.5e+06	5.1e+06	877	1076
45000	1	1.1e+07	2.2e+07	4489	5492
3100	2	2.2e+06	4.3e+06	527	804
10300	2	7.4e+06	1.4e+07	2036	3097
45000	2	3.2e+07	6.2e+07	10687	15965
3100	3	5.8e+06	9.4e+06	1246	1656
10300	3	1.9e+07	3.1e+07	5020	6600
45000	3	8.3e+07	1.3e+08	27228	34597
3100	4	1.2e+07	1.8e+07	1980	2749
10300	4	4.1e+07	5.9e+07	7372	10098
45000	4	1.8e+08	2.6e+08	37018	50297

Table 4.2: Number of non-zero terms in the global matrix and memory used.

# Mesh elements	Interpolation degree	Construction time (s)		Solution time (s)	
		Cent. scheme	Upw. scheme	Cent. scheme	Upw. scheme
3100	1	2.8e-02	4.0e-02	1.3	1.5
10300	1	9.9e-02	0.1	6.7	7.2
45000	1	0.4	0.7	48.4	68.0
3100	2	8.8e-02	0.1	4.1	6.0
10300	2	0.3	0.3	19.0	28.8
45000	2	1.3	1.5	155.0	224.5
3100	3	0.2	0.2	10.0	14.4
10300	3	0.7	0.8	50.5	78.2
45000	3	3.4	3.4	438.9	643.2
3100	4	0.5	0.5	18.0	28.1
10300	4	1.6	1.8	86.1	135.2
45000	4	11.7	7.6	915.3	1077.4

Table 4.3: Time required for the global matrix construction and for the system resolution.

h (m)	Interpolation degree	Mean Error V_x		Relative Error V_x	
		Cent. scheme	Upw. scheme	Cent. scheme	Upw. scheme
625.0	1	4.8e-02	1.8e-02	15.9	6.0
312.5	1	3.2e-03	1.7e-03	3.3	1.8
56.25	1	1.7e-04	9.9e-05	0.8	0.4
625.0	2	1.7e-03	1.6e-03	0.5	0.5
312.5	2	5.9e-05	5.7e-05	6.0e-02	5.8e-02
56.25	2	1.4e-06	1.4e-06	6.1e-03	6.1e-03
625.0	3	1.4e-04	1.3e-04	4.2e-02	4.1e-02
312.5	3	3.2e-06	3.1e-06	3.3e-03	3.2e-03
56.25	3	3.8e-08	3.7e-08	1.7e-04	1.7e-04
625.0	4	1.1e-05	1.0e-05	3.4e-03	3.2e-03
312.5	4	7.6e-08	6.8e-08	7.8e-05	7.0e-05
56.25	4	3.5e-10	3.1e-10	1.6e-06	1.4e-06

Table 4.4: Mean and relative errors on V_x.

h (m)	Interpolation degree	Mean Error σ_{xx}		Relative Error σ_{xx}		Convergence order	
		Cent. scheme	Upw. scheme	Cent. scheme	Upw. scheme	Cent. scheme	Upw. scheme
625.0	1	165.5	72.9	13.6	6.0	-	-
312.5	1	17.3	6.6	4.5	1.7	1.7	1.7
56.25	1	1.6	0.4	1.8	0.4	1.3	2.0
625.0	2	7.6	5.9	0.6	0.5	-	-
312.5	2	0.5	0.3	0.1	6.5e-02	2.3	2.9
56.25	2	2.2e-02	6.2e-03	2.5e-02	6.9e-03	2.3	3.2
625.0	3	0.8	0.4	6.4e-02	3.1e-02	-	-
312.5	3	3.8e-02	1.0e-02	9.8e-03	2.7e-03	2.8	3.7
56.25	3	9.5e-04	1.4e-04	1.1e-03	1.5e-04	3.2	4.2
625.0	4	5.9e-02	3.4e-02	4.6e-03	2.7e-03	-	-
312.5	4	1.1e-03	3.1e-04	2.8e-04	7.9e-05	4.1	5.2
56.25	4	1.2e-05	1.5e-06	1.3e-05	1.7e-06	4.4	5.6

Table 4.5: Mean and relative errors on σ_{xx} and convergence order.

4.2 Disk-shaped scatterer

We consider now the test problem of the scattering of a plane wave by an infinite elastic cylinder. The analytical solution of this problem is given in annex A. This test problem is a little bit more complicated than the previous one because of its geometry. The computational domain Ω is a ring shape between two circular boundaries: the inner circle with radius $a = 2000\ m$ which is associated to the free surface boundary Γ_a on which we apply the first condition of (2.2), and the outer circle with radius $b = 8000\ m$ corresponding to the boundary Γ_b which is assumed to be an artificial boundary and on which we apply the second condition of (2.2). The computational domain Ω is represented on fig. 4.15. The features of the homogeneous material are a mass density $\rho = 1.0\ 10^3\ kg.m^{-3}$, Lamé's coefficients $\lambda = 8\ MPa$ and $\mu = 4\ MPa$, which imply a velocity v_p equal to 4.0 $10^3\ m.s^{-1}$ and a $S-$waves velocity v_s equal to 2.0 $10^3\ m.s^{-1}$. The distance between circles the two of radius a and b such that it corresponds to 1.5 times the wavelength λ_o. We remind that $\lambda_o = \dfrac{v_p}{f}$, where f is the frequency. f is chosen equal to 4 Hz. We discretize the computational domain Ω into three unstructured meshes with respectively 1200, 5100 and 21 000 elements. Two of these meshes are shown on figs. 4.16 and 4.17; their characteristics are given in table 4.6. The numerical convergence is presented on fig. 4.18 for the centered DG and upwind DG formulations. We remark that we do not obtain the expected convergence orders for both schemes, and that the two schemes behave similarly. This is probably due to the fact that the geometric error dominates. Indeed, for this test problem, the curved boundaries are discretized by affine elements which a limitation for obtaining higher convergence orders.

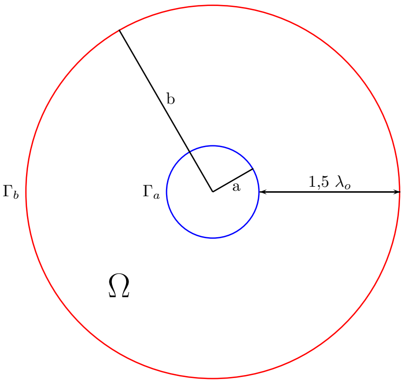

Figure 4.15: Configuration of the computational domain Ω for the elastic disk-shaped scatterer.

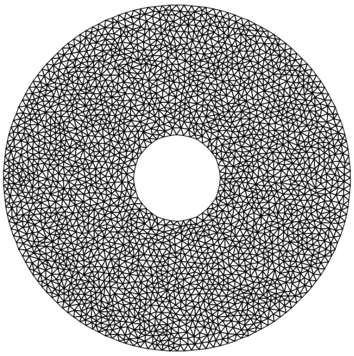

Figure 4.16: Discretization of the computational domain Ω for the elastic disk-shaped scatterer: mesh M1, 1200 elements.

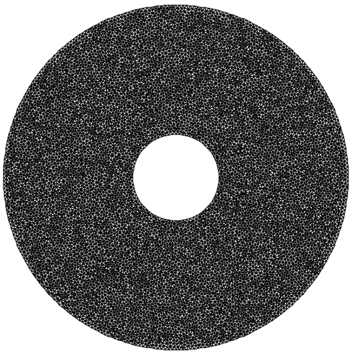

Figure 4.17: Discretization of the computational domain Ω for the elastic disk-shaped scatterer: mesh M2, 5100 elements.

Mesh	# Mesh elements	# Mesh vertices	h_{min}	h_{max}	h_{min}/h_{max}
M1	1200	640	440.5	1016.9	2.3
M2	5100	2630	212.4	490.1	2.3
M3	21 000	11 000	105.9	245.9	2.3

Table 4.6: Characteristics of the three meshes

On figs. 4.20 and 4.21 we plot the numerical solution for V_x component obtained respectively with the centered and upwind DGFD-$\mathbb{P}_2$ formulations on mesh M2 (with 5100 elements). We show the exact solution on fig. 4.19. It is interesting to look at the absolute error between the numerical solution and the exact solution (fig. 4.22 for the centered scheme and fig. 4.23 for the upwind scheme). As for the propagation of the plane wave in the homogeneous medium, we plot a 1D cut of the numerical solution (green cross), figs. 4.24 and 4.25 and we compare it to the exact solution (red line).

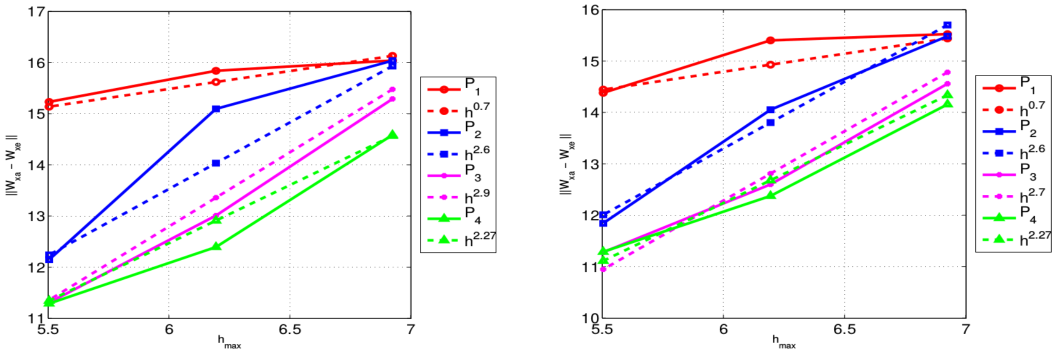

Figure 4.18: Convergence order of the centered (left) and upwind (right) flux DGFD methods for the elastic disk-shaped scatterer.

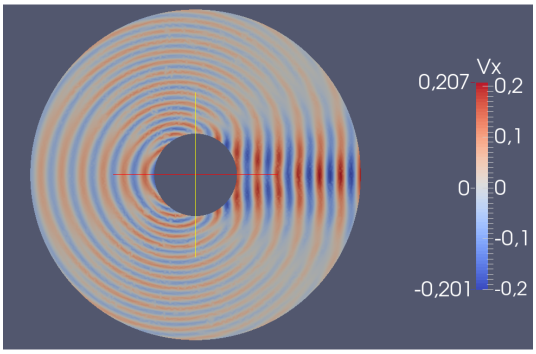

Figure 4.19: Exact solution of V_x for the elastic disk-shaped scatterer.

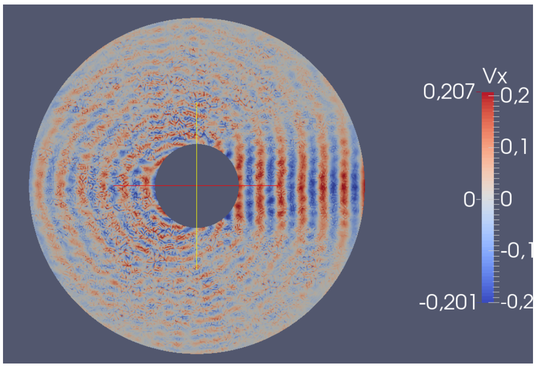

Figure 4.20: Numerical solution of V_x with the centered DGFD-$\mathbb{P}_2$ method for the elastic disk-shaped scatterer.

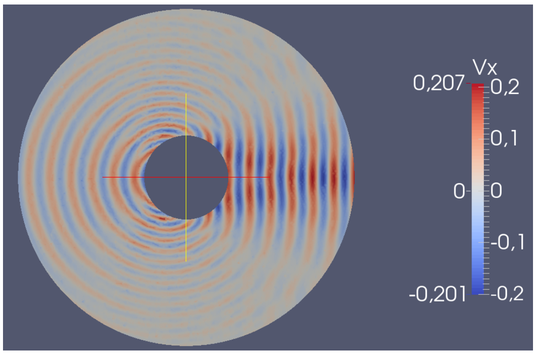

Figure 4.21: Numerical solution of V_x with the upwindd DGFD-$\mathbb{P}_2$ method for the elastic disk-shaped scatterer.

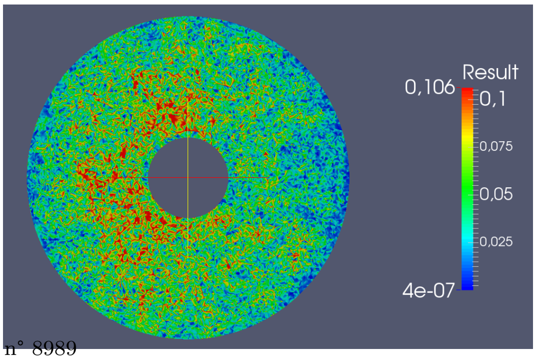

Figure 4.22: Absolute error between the exact solution and the solution computed with the centered DGFD-$\mathbb{P}_2$ method for the elastic disk-shaped scatterer.

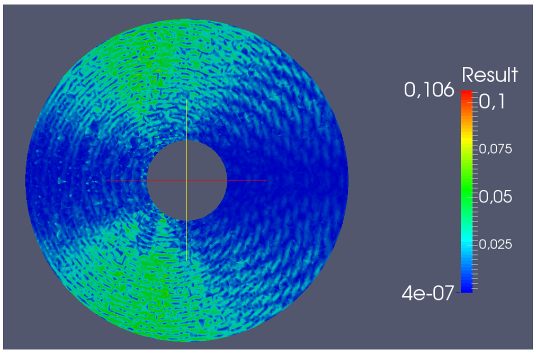

Figure 4.23: Absolute error between the exact solution and the solution computed with the upwind DGFD-$\mathbb{P}_2$ metho for the elastic disk-shaped scatterer.

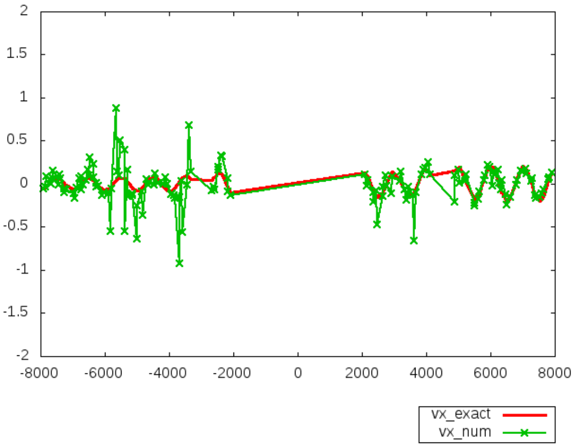

Figure 4.24: x-wise distribution V_x: centered DGFD-$\mathbb{P}_2$ solution for the elastic disk-shaped scatterer.

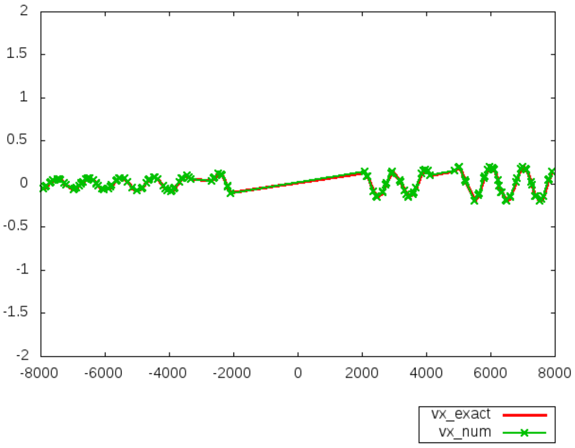

Figure 4.25: x-wise distribution of V_x: upwind DGFD-$\mathbb{P}_2$ solution for the elastic disk-shaped scatterer.

The computational performances of both methods are summarized in tables 4.7 for the number of non-zero terms in the global matrix and the memory used (in MB), 4.8 for the time required for the construction of the global matrix (in seconds) and for the resolution (in seconds) and 4.9-4.10 for the mean and relative errors on V_x and σ_{xx} components.

4.3 Elastic solid scatterer problem

Finally we consider the problem of the scattering of a plane wave by an elastic solid in an infinite circle, which corresponds to an heterogeneous wave propagation problem. The analytical solution of this problem is given in annex B. The computational domain $\Omega = \Omega_a \cup \Omega_b$ is represented

# Mesh elements	Interpolation degree	Non-zeros terms		Memory (MB)	
		Cent. scheme	Upw. scheme	Cent. scheme	Upw. scheme
1200	1	2.9e+05	5.9e+05	72	104
5100	1	1.2e+06	2.5e+06	379	496
21000	1	4.9e+06	1.0e+07	1895	2292
1200	2	8.6e+05	1.6e+06	180	269
5100	2	3.7e+06	7.0e+06	925	1360
21000	2	1.5e+07	2.7e+07	4361	6578
1200	3	2.2e+06	3.6e+06	391	525
5100	3	9.4e+06	1.5e+07	2154	2921
21000	3	3.8e+07	6.2e+07	11033	14131
1200	4	4.7e+06	6.8e+06	673	895
5100	4	2.0e+07	2.9e+07	3393	4537
21000	4	8.1e+07	1.2e+08	15679	21186

Table 4.7: Number of non-zero terms in the global matrix and memory used.

# Mesh elements	Interpolation degree	Construction time (s)		Solution time (s)	
		Cent. scheme	Upw. scheme	Cent. scheme	Upw. scheme
1200	1	1.1e-02	2.5e-02	0.4	0.7
5100	1	4.8e-02	0.1	2.5	4.0
21000	1	0.2	0.4	16.0	25.1
1200	2	3.5e-02	7.1e-2	1.3	2.6
5100	2	0.1	0.3	7.8	14.7
21000	2	0.6	1.2	47.7	93.7
1200	3	8.8e-02	0.2	2.9	5.3
5100	3	0.4	0.7	18.2	38.2
21000	3	1.5	2.7	129.4	249.3
1200	4	0.2	0.3	5.5	10.2
5100	4	0.8	1.4	33.6	65.6
21000	4	3.3	5.5	234.5	447.3

Table 4.8: Time required for the global matrix construction and for the system resolution.

h (m)	Interpolation degree	Mean Error V_x		Relative Error V_x	
		Cent. scheme	Upw. scheme	Cent. scheme	Upw. scheme
1016.9	1	1.7	1.1	276.5	175.4
490.1	1	0.4	0.2	219.4	131.6
245.9	1	5.6e-02	2.4e-2	113.6	47.1
1016.9	2	1.8	1.0	220.1	123.4
490.1	2	0.2	8.1e-2	81.1	36.8
245.9	2	1.7e-03	1.8e-3	3.0	3.2
1016.9	3	0.9	0.5	99.7	56.4
490.1	3	2.0e-02	1.6e-2	8.6	7.2
245.9	3	9.4e-04	9.6e-4	1.6	1.7
1016.9	4	0.5	0.4	47.6	37.3
490.1	4	1.2e-02	1.3e-2	5.5	5.5
245.9	4	9.9e-04	9.9e-4	1.7	1.7

Table 4.9: Mean and relative errors on V_x.

h (m)	Interpolation degree	Mean Error σ_{xx}		Relative Error σ_{xx}		Convergence order	
		Cent. scheme	Upw. scheme	Cent. scheme	Upw. scheme	Cent. scheme	Upw. scheme
1016.9	1	5950.9	3999.1	294.6	198.0	-	-
490.1	1	1001.7	829.2	166.1	137.5	0.3	0.2
245.9	1	133.3	66.1	74.4	36.9	0.9	1.5
1016.9	2	5673.7	3802.5	193.9	128.0	-	-
490.1	2	448.3	159.8	58.8	20.9	1.3	2.0
245.9	2	6.5	4.8	3.4	2.5	4.3	3.2
1016.9	3	2372.0	1195.1	72.0	36.3	-	-
490.1	3	56.5	37.9	7.3	4.9	3.1	2.7
245.9	3	3.1	3.0	1.6	1.5	2.5	1.9
1016.9	4	1141.6	743.8	34.3	22.3	-	-
490.1	4	31.6	31.0	4.1	3.4	3.0	2.4
245.9	4	3.0	3.0	1.5	1.5	1.6	1.6

Table 4.10: Mean and relative errors on σ_{xx} and convergence order.

on fig. 4.26. It is composed of the circle Ω_a and the ring Ω_b. We have two materials: the first material in Ω_b has a mass density $\rho = 1.0\ kg.m^{-3}$ and Lamé's coefficients $\lambda = 8.0\ MPa$ and $\mu = 4.0\ MPa$; the second material in Ω_a has a mass density $\rho = 2.0\ kg.m^{-3}$ and Lamé's coefficients $\lambda = 6.4\ 10^1\ MPa$ and $\mu = 3.2\ 10^1\ MPa$. These values imply a $P-$waves velocity v_p equal to $4.0\ 10^3\ m.s^{-1}$ in Ω_b and to $8.0\ 10^3\ m.s^{-1}$ in Ω_a, and a $S-$waves velocity v_s equal to $2.0\ 10^3\ m.s^{-1}$ in Ω_b and to $4.0\ 10^3\ m.s^{-1}$ in Ω_a. We discretize the computational domain Ω into three unstructured meshes with respectively 1300, 5400 and 22 000 elements. Two of these meshes are shown on figs. 4.27 and 4.28; their characteristics are given in table 4.11.

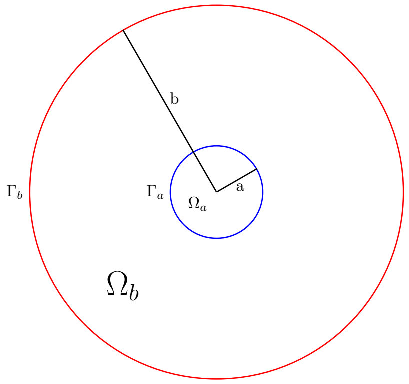

Figure 4.26: Configuration of the computational domain Ω for the elastic solid scatterer.

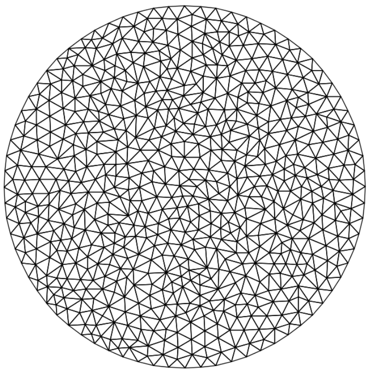

Figure 4.27: Discretization of the computational domain Ω for the elastic solid scatterer: mesh M1, 1300 elements.

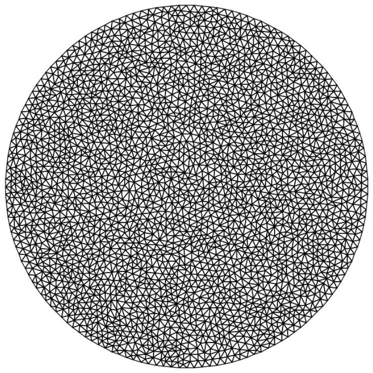

Figure 4.28: Discretization of the computational domain Ω for the elastic solid scatterer: mesh M2, 5400 elements.

The numerical convergence is presented on fig. 4.29 for the centered DG and upwind DG formulations. We obtain the same numerical convergence for both methods as with the previous test problem.

On figs. 4.31 and 4.32 we plot the numerical solution for V_x component obtained respectively with the centered and upwind DGFD-$\mathbb{P}_2$ formulations on mesh M2 (with 5100 elements). We show the exact solution on fig. 4.30. We plot the absolute error between the numerical solution

Mesh	# Mesh elements	# Mesh vertices	h_{min}	h_{max}	h_{min}/h_{max}
M1	1300	700	440.5	1016.9	2.3
M2	5400	2800	211.6	490.1	2.3
M3	22 000	11 000	105.9	245.9	2.3

Table 4.11: Characteristics of the three meshes

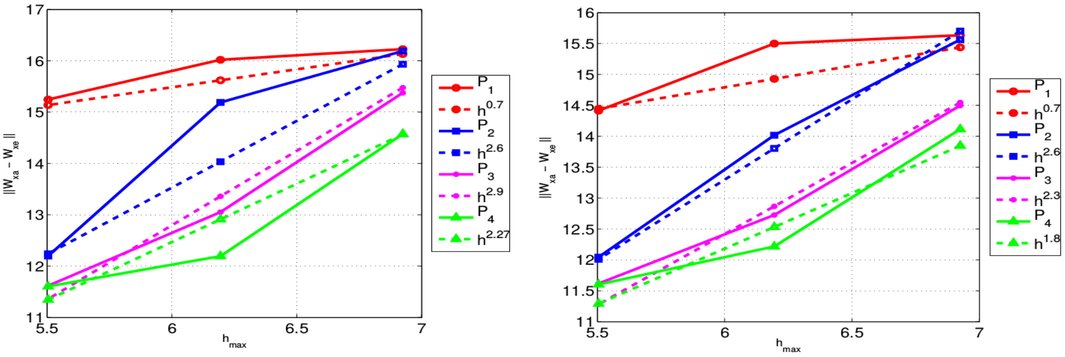

Figure 4.29: Convergence order of the centered (left) and upwind (right) flux DGFD methods for the elastic solid scatterer.

and the exact solution on fig. 4.33 for the centered scheme and on fig. 4.34 for the upwind scheme. As we have done with the two previous test problems, we plot a 1D cut of the numerical solution (green cross), fig. 4.35 and 4.36 and we compare it to the exact solution (red line).

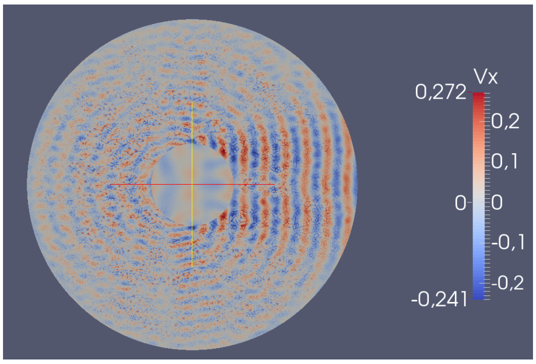

Figure 4.31: Numerical solution of V_x with the centered DGFD-$\mathbb{P}_2$ method for the elastic solid scatterer.

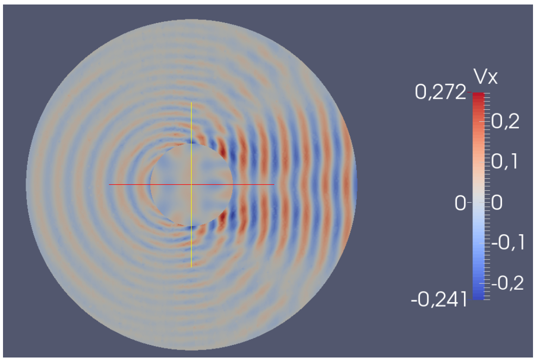

Figure 4.32: Numerical solution of V_x with the upwind DGFD-$\mathbb{P}_2$ method for the elastic solid scatterer.

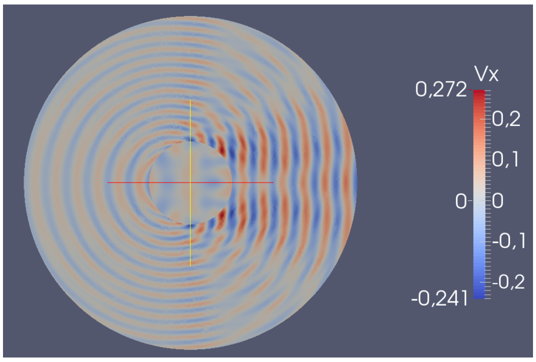

Figure 4.30: Exact solution of V_x for the elastic solid scatterer.

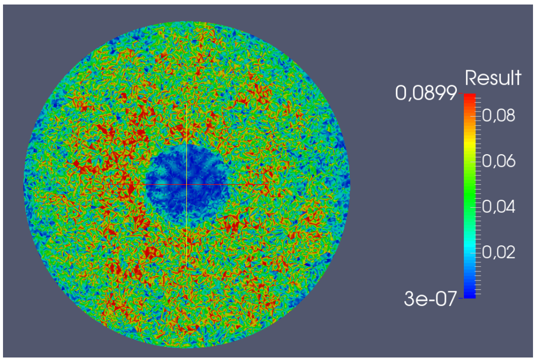

Figure 4.33: Absolute error between the exact solution and the solution computed with the centered DGFD-$\mathbb{P}_2$ method for the elastic solid scatterer.

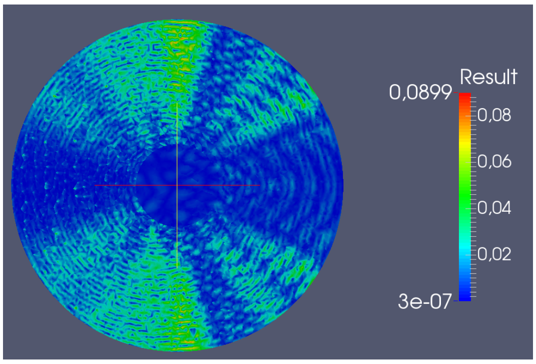

Figure 4.34: Absolute error between the exact solution and the solution computed with the upwind DGFD-$\mathbb{P}_2$ method for the elastic solid scatterer.

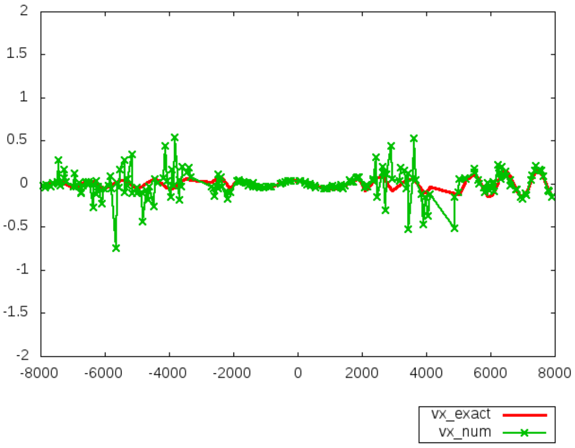

Figure 4.35: x-wise distribution V_x: centered DGFD-$\mathbb{P}_2$ solution for the elastic solid scatterer.

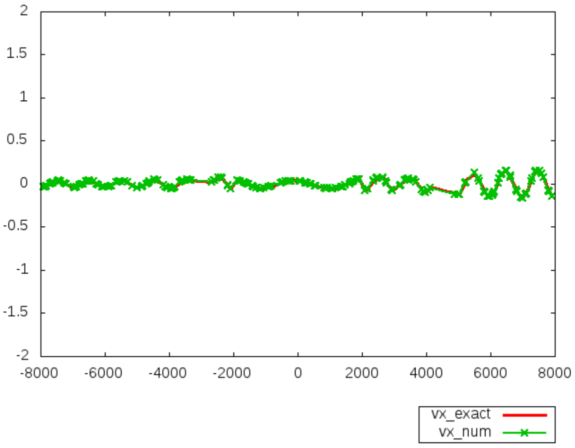

Figure 4.36: x-wise distribution of V_x: upwind DGFD-$\mathbb{P}_2$ solution for the elastic solid scatterer.

The computational performances of both methods are summarized in tables 4.12 for the number of non-zero terms in the global matrix and the memory used (in MB), 4.13 for the time required for the construction of the global matrix (in seconds) and for the resolution (in seconds) and 4.14-4.15 for the mean and relative errors on V_x and σ_{xx} components.

# Mesh elements	Interpolation degree	Non-zeros terms		Memory (MB)	
		Cent. scheme	Upw. scheme	Cent. scheme	Upw. scheme
1300	1	307524	628307	80	111
5400	1	1313566	2695385	433	548
22000	1	5262206	10831799	2118	2607
1300	2	917268	1753016	198	307
5400	2	3908177	7511693	1029	1543
22000	2	15659108	30172014	4968	7318
1300	3	2367116	3818526	441	604
5400	3	10089405	16342985	2432	3233
22000	3	40427302	65620155	12422	15741
1300	4	5040880	7279634	743	988
5400	4	21485679	31137145	3751	5160
22000	4	86107211	124983019	17407	23982

Table 4.12: Number of non-zero terms in the global matrix and memory used.

# Mesh elements	Interpolation degree	Construction time (s)		Solution time (s)	
		Cent. scheme	Upw. scheme	Cent. scheme	Upw. scheme
1300	1	1.2e-02	1.8e-02	0.5	0.5
5400	1	5.0e-02	8.0e-02	3.0	3.6
22000	1	0.2	0.3	19.9	26.6
1300	2	3.7e-02	4.7e-02	1.4	2.3
5400	2	0.2	0.2	9.1	14.4
22000	2	0.6	0.8	64.7	98.2
1300	3	9.5e-02	0.1	3.4	5.1
5400	3	0.4	0.5	22.6	36.7
22000	3	1.6	1.9	167.3	348.1
1300	4	0.2	0.2	6.4	9.2
5400	4	0.9	1.0	40.4	69.6
22000	4	3.4	3.8	283.4	525.4

Table 4.13: Time required for the global matrix construction and for the system resolution.

h (m)	Interpolation degree	Mean Error V_x		Relative Error V_x	
		Cent. scheme	Upw. scheme	Cent. scheme	Upw. scheme
1016.9	1	1.7	1.0	291.9	170.2
490.1	1	0.3	0.2	217.2	125.5
245.9	1	4.9e-02	2.0e-02	102.0	41.8
1016.9	2	1.7	0.9	221.8	120.1
490.1	2	0.2	6.4e-02	86.7	31.0
245.9	2	1.6e-03	1.7e-03	3.0	3.3
1016.9	3	0.8	0.4	95.4	46.4
490.1	3	1.8e-02	1.4e-02	8.5	6.5
245.9	3	9.7e-04	9.9e-04	1.8	1.9
1016.9	4	0.4	0.3	42.7	29.9
490.1	4	7.2e-03	7.7e-03	3.4	3.6
245.9	4	9.9e-04	9.9e-04	1.9	1.9

Table 4.14: Mean and relative errors on V_x.

h (m)	Interpolation degree	Mean Error σ_{xx}		Relative Error σ_{xx}		Convergence order	
		Cent. scheme	Upw. scheme	Cent. scheme	Upw. scheme	Cent. scheme	Upw. scheme
1016.9	1	6482.2	4119.1	261.3	166.1	-	-
490.1	1	1125.5	830.8	154.0	113.7	0.3	0.2
245.9	1	125.8	63.9	60.2	30.6	1.1	1.6
1016.9	2	5934.8	3742.9	172.1	108.6	-	-
490.1	2	459.3	143.2	52.5	16.4	1.4	2.1
245.9	2	6.3	5.5	2.9	2.5	4.3	2.9
1016.9	3	2353.6	1054.3	62.4	27.9	-	-
490.1	3	56.0	41.6	6.3	4.7	3.2	2.4
245.9	3	3.9	3.9	1.7	1.7	2.1	1.6
1016.9	4	1073.5	667.3	28.3	17.6	-	-
490.1	4	26.4	26.9	3.0	3.0	3.3	2.6
245.9	4	3.8	3.8	1.7	1.7	0.9	0.9

Table 4.15: Mean and relative errors on σ_{xx} and convergence order.

5 Conclusion

In this report, we studied two nodal DG methods, the centered flux DG method and the upwind flux DG method, for the solution of the 2D elastic Helmholtz equations. We numerically observed that the centered DG formulation is suboptimal in terms of convergence speed as compared to a classical FE method or the upwind DG formulation considered here. Moreover accuracy results are generally better with the upwind flux DG method for a given mesh. Indeed, the upwind DG method is more accurate than the centered DG one whatever is the computational domain configuration or the medium complexity.

However the upwind DG scheme required more memory space (around 1,5 times much memory) and computational time (around twice much time). This is due to the fact that, in the upwind flux case, the number of non-zero terms in the discretematric operator is around twice as important as the one of the centered method.

The facts that the centered DG method is not enough accurate and the upwind DG method is expensive in terms of memory and computational time, motivate the study of an alternative DG formulation: the hybridizable DG (HDG) method. In a subsequent report, we present and study numerically such a HDG method the 2D elastic Helmholtz equations and we compare the HDG results with those obtained with upwind DG method which we consider as a reference method for our study.

Acknowledgements

The authors acknowledge the support by the INRIA-TOTAL strategic action DIP (dip.inria.fr).

References

[1] Michel Kern. *Problèmes inverses: aspects numériques.* 2002.

[2] Jean Virieux, Vincent Etienne, and Victor Cruz-Atienza. Modelling seismic wave propagation for geophysical imaging. *Seismic Waves, Research and Analysis*, pages 253–304, 2012.

[3] Romain Brossier. *Imagerie sismique à deux dimensions des milieux visco-élastiques par inversion des formes d'ondes: développements méthodologiques et applications.* PhD thesis, Université de Nice-Sophia Antipolis, nov 2009.

[4] Sarah Delcourte, Loula Fezoui, and Nathalie Glinsky-Olivier. A high order discontinuous Galerkin method for the seismic wave propagation. *ESAIM: Proceedings*, 27:70–89, may 2009.

[5] Stéphane Lanteri and Mohamed El Bouajaji. High order discontinuous Galerkin method for the solution of 2D time-harmonic Maxwell's equations. *Applied Mathematics and Computation*, 219:7241–7251, 2013.

[6] Michael Dumbser and Martin Martin Käser. An arbitrary high-order discontinuous Galerkin method for elastic waves on unstructured meshes - II. The three-dimensional isotropic case. *Geophysical Journal International*, 167:319–336, 2006.

[7] Patrick Amestoy, Iain Duff, and Jean-Yves L'Excellent. Multifrontal parallel distributed symmetric and unsymmetric solvers. *Computationnal Methods in Applied Mechanics and Engineering*, 184:501–520, 2000.

[8] Josep de la Puente, Martin Käser, Michael Dumbser, and Heine Igel. An arbitrary high-order discontinuous Galerkin method for elastic waves on unstructured meshes - IV. Anisotropy. *Geophysical Journal International*, 169:1210–1228, 2007.

[9] Mark Ainsworth, Peter Monk, and Wagner Muniz. Dispersive and dissipative properties of discontinuous Galerkin finite element methods for the second-order wave equation. *Journal of Scientific Computing*, 27(1–3):5–40, jun 2006.

A Analytical solution of the disk-shaped scatterer problem

In this section, we recall the analytical expression of the solution for the problem of the scattering of a plane wave by an elastic disk-shaped configuration. This analytical solution is expressed in the form of Fourier series. In the case of an infinite solid domain, the total displacement field u can be expressed using two others displacement fields u^1 and u^2 as

$$u = u^1 + u^2. \tag{A.1}$$

Each of these displacement fields u^j, $j = 1, 2$, can be written with the help of two potentials ϕ^j and ψ^j

$$u^1 = \nabla\phi^1 + (-\mathbf{e_z}) \times \nabla\psi^1, \tag{A.2}$$
$$u^2 = \nabla\phi^2 + (-\mathbf{e_z}) \times \nabla\psi^2, \tag{A.3}$$

where

$$\phi^1 = \sum_{n=0}^{+\infty} A_n^1 H_n^{(1)}(k_p r)\cos(n\theta), \qquad \psi^1 = \sum_{n=0}^{+\infty} A_n^2 H_n^{(1)}(k_s r)\sin(n\theta),$$
$$\phi^2 = \sum_{n=0}^{+\infty} A_n^3 H_n^{(2)}(k_p r)\cos(n\theta), \qquad \psi^2 = \sum_{n=0}^{+\infty} A_n^4 H_n^{(2)}(k_s r)\sin(n\theta),$$

and $\mathbf{e_z}$ is the third vector of the cartesian basis. $H_n^{(1)}$ and $H_n^{(2)}$ respectively represent Hankel's functions of first and second kind, defined such as

$$\begin{aligned} H_n^{(1)}(x) &= J_n(x) + iY_n(x) \\ H_n^{(2)}(x) &= J_n(x) - iY_n(x). \end{aligned} \tag{A.4}$$

The Hankel function of second kind is the conjugate of the Hankel function of first kind. J_n and Y_n are respectively Bessel's functions of first and second kind. $k_p = \dfrac{\omega}{v_p}$ is the $P-$wave number and $k_s = \dfrac{\omega}{v_s}$ the $S-$wave number. In polar coordinates, we have

$$\nabla\phi^j = \frac{\partial\phi^j}{\partial r}\mathbf{e_r} + \frac{1}{r}\frac{\partial\phi^j}{\partial\theta}\mathbf{e}_\theta, \qquad j = 1, 2,$$
$$(-\mathbf{e_z}) \times \nabla\psi^j = \frac{1}{r}\frac{\partial\psi^j}{\partial\theta}\mathbf{e_r} - \frac{\partial\psi^j}{\partial r}\mathbf{e}_\theta, \qquad j = 1, 2.$$

This allows us to write

$$u^j = u_r^j\mathbf{e_r} + u_\theta^j\mathbf{e}_\theta, \tag{A.5}$$
$$u = \left(u_r^1 + u_r^2\right)\mathbf{e_r} + \left(u_\theta^1 + u_\theta^2\right)\mathbf{e}_\theta, \tag{A.6}$$

where $\quad u_r^j = \dfrac{\partial\phi^j}{\partial r} + \dfrac{1}{r}\dfrac{\partial\psi^j}{\partial\theta} \quad$ and $\quad u_\theta^j = \dfrac{1}{r}\dfrac{\partial\phi^j}{\partial\theta} - \dfrac{\partial\psi^j}{\partial r}.$

Since the polar basis vectors $\mathbf{e_r}$ and $\mathbf{e}_\theta$ are given in the cartesian basis by $(\cos\theta, \sin\theta)^t$ and $(-\sin\theta, \cos\theta)^t$ respectively, it follows that the components of the displacement field can be expressed in the cartesian basis as

$$\left\{ \begin{array}{lclcl} u_x &=& u_r\cos\theta - u_\theta\sin\theta &=& (u_r^1 + u_r^2)\cos\theta - (u_\theta^1 + u_\theta^2)\sin\theta, \\ u_z &=& u_r\sin\theta + u_\theta\cos\theta &=& (u_r^1 + u_r^2)\sin\theta + (u_\theta^1 + u_\theta^2)\cos\theta, \end{array} \right. \tag{A.7}$$

with

$$u_r^1 = \sum_{n=0}^{+\infty} \left[A_n^1 k_p H_n^{(1)'}(k_p r) + \frac{n}{r} A_n^2 H_n^{(1)}(k_s r) \right] \cos(n\theta),$$

$$u_\theta^1 = \sum_{n=0}^{+\infty} \left[-A_n^1 \frac{n}{r} H_n^{(1)}(k_p r) - A_n^2 k_s H_n^{(1)'}(k_s r) \right] \sin(n\theta),$$

$$u_r^2 = \sum_{n=0}^{+\infty} \left[A_n^3 k_p H_n^{(2)'}(k_p r) + \frac{n}{r} A_n^4 H_n^{(2)}(k_s r) \right] \cos(n\theta),$$

$$u_\theta^2 = \sum_{n=0}^{+\infty} \left[-A_n^3 \frac{n}{r} H_n^{(2)}(k_p r) - A_n^4 k_s H_n^{(2)'}(k_s r) \right] \sin(n\theta).$$

Knowing that derivatives of Hankel's functions are determined by one of the two recurrence relations

$$H_n^{(j)'}(x) = \begin{cases} -H_{n+1}^{(j)}(x) & \text{for } n = 0, \\ H_{n-1}^{(j)}(x) - \dfrac{n}{x} H_n^{(j)}(x) & \text{for } n > 0, \end{cases}$$

or

$$H_n^{(j)'}(x) = \begin{cases} -H_{n+1}^{(j)}(x) & \text{for } n = 0, \\ -H_{n+1}^{(j)}(x) + \dfrac{n}{x} H_n^{(j)}(x) & \text{for } n > 0, \end{cases}$$

we choose to write arbitrarily

$$H_n^{(1)'}(x) = \begin{cases} -H_{n+1}^{(1)}(x) & \text{for } n = 0, \\ -H_{n+1}^{(1)}(x) + \dfrac{n}{x} H_n^{(1)}(x) & \text{for } n > 0, \end{cases}$$

and

$$H_n^{(2)'}(x) = \begin{cases} -H_{n+1}^{(2)}(x) & \text{for } n = 0, \\ H_{n-1}^{(2)}(x) - \dfrac{n}{x} H_n^{(2)}(x) & \text{for } n > 0. \end{cases}$$

Finally this leads to

$$\begin{aligned} u_r &= \sum_{n=0}^{+\infty} \left[A_n^1 k_p H_n^{(1)'}(k_p r) + A_n^2 \frac{n}{r} H_n^{(1)}(k_s r) + A_n^3 k_p H_n^{(2)'}(k_p r) + A_n^4 \frac{n}{r} H_n^{(2)}(k_s r) \right] \cos(n\theta) \\ u_\theta &= \sum_{n=0}^{+\infty} \left[-A_n^1 \frac{n}{r} H_n^{(1)}(k_p r) - A_n^2 k_s H_n^{(1)'}(k_s r) - A_n^3 \frac{n}{r} H_n^{(2)}(k_p r) - A_n^4 k_s H_n^{(2)'}(k_s r) \right] \sin(n\theta). \end{aligned} \tag{A.8}$$

In order to determine coefficients A_n^1, A_n^2, A_n^3 and A_n^4, we have to use the boundary conditions. We get

$$u = -u^{inc} \qquad \text{on } \Gamma_a, \tag{A.9}$$

$$\underline{\underline{\sigma}}\mathbf{n} = v_p \left(\mathbf{v} \cdot \mathbf{n}\right) \mathbf{n} + v_s \left(\mathbf{v} \cdot \mathbf{t}\right) \mathbf{t} \qquad \text{on } \Gamma_b. \tag{A.10}$$

We recall the reader to refer to figure 4.15 for the definition of the boundaries Γ_a and Γ_b. u^{inc} is the incident wave which is written as

$$u^{inc} = \nabla\phi^{inc} + (-\mathbf{e_z}) \times \nabla\psi^{inc},$$

with $\psi^{inc} = 0$ and

$$\phi^{inc} = \sum_{n=0}^{+\infty} \varepsilon_n i^n J_n(k_p r)\cos(n\theta)$$

where $\varepsilon_n = \begin{cases} 1 & \text{if } n = 0, \\ 2 & \text{if } n \geq 1, \end{cases}$. And finally we write

$$\begin{aligned} u^{inc} &= \frac{\partial \phi^{inc}}{\partial r}\mathbf{e_r} + \frac{1}{r}\frac{\partial \phi^{inc}}{\partial \theta}\mathbf{e}_\theta \\ &= \sum_{n=0}^{+\infty} \varepsilon_n i^n \cos(n\theta) k_p J_n'(k_p r)\mathbf{e_r} + \sum_{n=0}^{+\infty} \frac{-n}{r}\varepsilon_n i^n J_n(k_p r)\sin(n\theta)\mathbf{e}_\theta. \end{aligned} \tag{A.11}$$

If we develop the equation

$$\underline{\underline{\sigma}}\mathbf{n} = v_p\left(\mathbf{v}\cdot\mathbf{n}\right)\mathbf{n} + v_s\left(\mathbf{v}\cdot\mathbf{t}\right)\mathbf{t},$$

in polar coordinates, we find

$$\begin{array}{rcl} \sigma_{rr} & = & i\omega\rho v_p u_r, \\ \sigma_{r\theta} & = & i\omega\rho v_s u_\theta. \end{array} \tag{A.12}$$

σ_{rr} and $\sigma_{r\theta}$ can be expressed in terms of potentials ψ^j et ϕ^j

$$\begin{array}{rcccl} \sigma_{rr} & = & \sigma^1_{rr} + \sigma^2_{rr} & = & \displaystyle\sum_{j=1,2} \sigma^{\phi^j}_{rr} + \sigma^{\psi^j}_{rr}, \\ \sigma_{r\theta} & = & \sigma^1_{r\theta} + \sigma^2_{r\theta} & = & \displaystyle\sum_{j=1,2} \sigma^{\phi^j}_{r\theta} + \sigma^{\psi^j}_{r\theta}, \end{array} \tag{A.13}$$

where

$$\begin{aligned} \sigma^{\phi^j}_{rr} &= \lambda\Delta\phi^j + 2\mu\frac{\partial^2\phi^j}{\partial r^2}, \\ \sigma^{\psi^j}_{rr} &= 2\mu\left[\frac{\partial}{\partial r}\left(\frac{1}{r}\frac{\partial\psi^j}{\partial\theta}\right)\right], \\ \sigma^{\phi^j}_{r\theta} &= 2\mu\left(\frac{1}{r}\frac{\partial^2\phi^j}{\partial\theta\partial r} - \frac{1}{r^2}\frac{\partial\phi^j}{\partial\theta}\right), \\ \sigma^{\psi^j}_{r\theta} &= \mu\left[\frac{1}{r^2}\frac{\partial^2\psi^j}{\partial\theta^2} - r\frac{\partial}{\partial r}\left(\frac{1}{r}\frac{\partial\psi^j}{\partial r}\right)\right]. \end{aligned}$$

where ϕ^j satisfies the Helmholtz equation

$$\Delta\phi^j = -k_p^2\phi^j.$$

This yields

$$\Delta\phi^j = -k_p^2\sum_{n=0}^{+\infty} A_n^h H_n^{(j)}(k_p r)\cos(n\theta), \quad h = 1 \text{ or } 3.$$

Then, by some calculations, we obtain

$$
\begin{aligned}
\frac{\partial^2\phi^j}{\partial r^2} &= \sum_{n=0}^{+\infty} A_n^h k_p^2 H_n^{(j)''}(k_p r)\cos(n\theta),\\
\frac{\partial}{\partial r}\left(\frac{1}{r}\frac{\partial\psi^j}{\partial\theta}\right) &= -\frac{1}{r^2}\frac{\partial\psi^j}{\partial\theta}+\frac{1}{r}\frac{\partial^2\psi^j}{\partial r\partial\theta}\\
&= -\frac{1}{r^2}\sum_{n=0}^{+\infty} A_n^l H_n^{(j)}(k_s r)(n\cos(n\theta))\\
&+ \tfrac{1}{r}\textstyle\sum_{n=0}^{+\infty} nA_n^l k_s H_n^{(j)'}(k_s r)\cos(n\theta), \quad l = 2 \text{ ou } 4,\\
\frac{\partial^2\phi^j}{\partial\theta\partial r} &= \sum_{n=0}^{+\infty} A_n^h k_p H_n^{(j)'}(k_p r)\left(-n\sin(n\theta)\right),\\
\frac{\partial\phi^j}{\partial\theta} &= \sum_{n=0}^{+\infty} A_n^h H_n^{(j)}(k_p r)\left(-n\sin(n\theta)\right),\\
\frac{\partial^2\psi^j}{\partial\theta^2} &= \sum_{n=0}^{+\infty} A_n^l H_n^{(j)}(k_s r)(-n^2\sin(n\theta)),\\
\frac{\partial}{\partial r}\left(\frac{1}{r}\frac{\partial\psi^j}{\partial r}\right) &= -\frac{1}{r^2}\frac{\partial\psi^j}{\partial r}+\frac{1}{r}\frac{\partial^2\psi^j}{\partial r^2}\\
&= -\frac{1}{r^2}\sum_{n=0}^{+\infty} A_n^l k_s H_n^{(j)'}(k_s r)\sin(n\theta)+\frac{1}{r}\sum_{n=0}^{+\infty} A_n^l k_s^2 H_n^{(j)''}(k_s r)\sin(n\theta).
\end{aligned}
$$

In summary, for $\underline{\underline{\sigma}}^1$, we get

$$
\left\{
\begin{aligned}
\sigma_{rr}^1 &= \sum_{n=0}^{+\infty}\Big[A_n^1 k_p^2\left(-\lambda H_n^{(1)}(k_p r)+2\mu H_n^{(1)''}(k_p r)\right)+\\
&\qquad A_n^2\frac{2\mu n}{r}\left(-\frac{1}{r}H_n^{(1)}(k_s r)+k_s H_n^{(1)'}(k_s r)\right)\Big]\cos(n\theta),\\
\sigma_{r\theta}^1 &= \mu\sum_{n=0}^{+\infty}\Big[-2A_n^1\frac{n}{r}\left(k_p H_n^{(1)'}(k_p r)-\frac{1}{r}H_n^{(1)}(k_p r)\right)+\\
&\qquad A_n^2\left(-\frac{n^2}{r^2}H_n^{(1)}(k_s r)+\frac{1}{r}k_s H_n^{(1)'}(k_s r)-k_s^2 H_n^{(1)''}(k_s r)\right)\Big]\sin(n\theta).
\end{aligned}
\right.
\tag{A.14}
$$

In addition, since $k_p^2(\lambda+2\mu)=k_s^2\mu$, we obtain $\lambda=\dfrac{k_s^2}{k_p^2}\mu-2\mu$. Moreover, we remark that

$$
\begin{aligned}
H_n^{(1)''}(k_p r) &= -\frac{1}{k_p r}H_n^{(1)'}(k_p r)-(1-\frac{n^2}{(k_p r)^2})H_n^{(1)}(k_p r)\\
&= \frac{1}{k_p r}H_{n+1}^{(1)}(k_p r)-\frac{n}{(k_p r)^2}H_n^{(1)}(k_p r)-(1-\frac{n^2}{(k_p r)^2})H_n^{(1)}(k_p r).
\end{aligned}
$$

It follows that

$$\left\{\begin{array}{lcl}\sigma^1_{rr} & = & \displaystyle\sum_{n=0}^{+\infty}\left[A^1_n\frac{2\mu}{r^2}\left(\left(n^2-n-\frac{1}{2}k_p^2r^2\right)H_n^{(1)}(k_pr)+k_prH_{n+1}^{(1)}(k_pr)\right)+\right.\\ & & \displaystyle\left.A^2_n\frac{2\mu n}{r^2}\left((n-1)\,H_n^{(1)}(k_sr)-k_srH_{n+1}^{(1)}(k_pr)\right)\right]\cos(n\theta),\\ \sigma^1_{r\theta} & = & \displaystyle\sum_{n=0}^{+\infty}\left[-A^1_n\frac{2\mu n}{r^2}\left((n-1)\,H_n^{(1)}(k_pr)-k_prH_{n+1}^{(1)}(k_pr)\right)-\right.\\ & & \displaystyle\left.A^2_n\frac{2\mu}{r^2}\left(\left(n^2-n-\frac{1}{2}k_s^2r^2\right)H_n^{(1)}(k_sr)+k_srH_{n+1}^{(1)}(k_sr)\right)\right]\sin(n\theta).\end{array}\right. \tag{A.15}$$

We can do the same for $\underline{\underline{\sigma}}^2$ and we obtain

$$\left\{\begin{array}{lcl}\sigma^2_{rr} & = & \displaystyle\sum_{n=0}^{+\infty}\left[-A^3_n\mu\left(\left(k_s^2-2k_p^2\right)H_n^{(2)}(k_pr)+2k_p^2H_n^{(2)''}(k_pr)\right)+\right.\\ & & \displaystyle\left.2A^4_n\mu\frac{n}{r}\left(\frac{-1}{r}H_n^{(2)}(k_sr)+k_sH_n^{(2)'}(k_sr)\right)\right]\cos(n\theta),\\ \sigma^2_{r\theta} & = & \displaystyle\sum_{n=0}^{+\infty}\left[-2A^3_n\mu\frac{n}{r}\left(k_pH_n^{(2)'}(k_pr)-\frac{1}{r}H_n^{(2)}(k_pr)\right)+\right.\\ & & \displaystyle\left.A^4_n\mu\left(-\frac{n^2}{r^2}H_n^{(2)}(k_sr)+\frac{1}{r}k_sH_n^{(2)'}(k_sr)-k_s^2H_n^{(2)''}(k_sr)\right)\right]\sin(n\theta).\end{array}\right. \tag{A.16}$$

If we sum these two systems, we finally get for $\underline{\underline{\sigma}}$

$$\left\{\begin{array}{lcl}\sigma_{rr} & = & \displaystyle\sum_{n=0}^{+\infty}\left[A^1_n\frac{2\mu}{r^2}\left(\left(n^2-n-\frac{1}{2}k_p^2r^2\right)H_n^{(1)}(k_pr)+k_prH_{n+1}^{(1)}(k_pr)\right)+\right.\\ & & \displaystyle A^2_n\frac{2\mu n}{r^2}\left((n-1)\,H_n^{(1)}(k_sr)-k_srH_{n+1}^{(1)}(k_pr)\right)-\\ & & \displaystyle A^3_n\mu\left(\left(k_s^2-2k_p^2\right)H_n^{(2)}(k_pr)+2k_p^2H_n^{(2)''}(k_pr)\right)+\\ & & \displaystyle\left.2A^4_n\mu\frac{n}{r}\left(\frac{-1}{r}H_n^{(2)}(k_sr)+k_sH_n^{(2)'}(k_sr)\right)\right]\cos(n\theta),\\ \sigma_{r\theta} & = & \displaystyle\sum_{n=0}^{+\infty}\left[-A^1_n\frac{2\mu n}{r^2}\left((n-1)\,H_n^{(1)}(k_pr)-k_prH_{n+1}^{(1)}(k_pr)\right)-\right.\\ & & \displaystyle A^2_n\frac{2\mu}{r^2}\left(\left(n^2-n-\frac{1}{2}k_s^2r^2\right)H_n^{(1)}(k_sr)+k_srH_{n+1}^{(1)}(k_sr)\right)-\\ & & \displaystyle 2A^3_n\mu\frac{n}{r}\left(k_pH_n^{(2)'}(k_pr)-\frac{1}{r}H_n^{(2)}(k_pr)\right)+\\ & & \displaystyle\left.A^4_n\mu\left(-\frac{n^2}{r^2}H_n^{(2)}(k_sr)+\frac{1}{r}k_sH_n^{(2)'}(k_sr)-k_s^2H_n^{(2)''}(k_sr)\right)\right]\sin(n\theta).\end{array}\right. \tag{A.17}$$

To summarize, using boundary conditions, we get

- At $r = a$,

$$\sum_{n=0}^{+\infty}\left[A^1_nk_pH_n^{(1)'}(k_pr)+A^2_n\frac{n}{r}H_n^{(1)}(k_sr)+A^3_nk_pH_n^{(2)'}(k_pr)+A^4_n\frac{n}{r}H_n^{(2)}(k_sr)\right]\cos(n\theta)=$$
$$-\sum_{n=0}^{+\infty}\varepsilon_ni^nk_pJ_n'(k_pr)\cos(n\theta), \tag{A.18}$$

$$\sum_{n=0}^{+\infty}\left[-A_n^1\frac{n}{r}H_n^{(1)}(k_pr)-A_n^2k_sH_n^{(1)'}(k_sr)-A_n^3\frac{n}{r}H_n^{(2)}(k_pr)-A_n^4k_sH_n^{(2)'}(k_sr)\right]\sin(n\theta)= \sum_{n=0}^{+\infty}\frac{n}{r}\varepsilon_n i^n J_n(k_pr)\sin(n\theta). \tag{A.19}$$

- At $r=b$,

$$\begin{aligned}
&\sum_{n=0}^{+\infty}\Bigg[A_n^1\frac{2\mu}{r^2}\left(\left(n^2-n-\frac{1}{2}k_p^2r^2\right)H_n^{(1)}(k_pr)+k_prH_{n+1}^{(1)}(k_pr)\right)+\\
&\qquad A_n^2\frac{2\mu n}{r^2}\left((n-1)\,H_n^{(1)}(k_sr)-k_srH_{n+1}^{(1)}(k_pr)\right)-\\
&\qquad A_n^3\mu\left(\left(k_s^2-2k_p^2\right)H_n^{(2)}(k_pr)+2k_p^2H_n^{(2)''}(k_pr)\right)+\\
&\qquad 2A_n^4\mu\frac{n}{r}\left(\frac{-1}{r}H_n^{(2)}(k_sr)+k_sH_n^{(2)'}(k_sr)\right)\Bigg]\cos(n\theta)=\\
&i\omega\rho v_p\sum_{n=0}^{+\infty}\left[A_n^1k_pH_n^{(1)'}(k_pr)+A_n^2\frac{n}{r}H_n^{(1)}(k_sr)+A_n^3k_pH_n^{(2)'}(k_pr)+A_n^4\frac{n}{r}H_n^{(2)}(k_sr)\right]\cos(n\theta),
\end{aligned} \tag{A.20}$$

$$\begin{aligned}
&\sum_{n=0}^{+\infty}\Bigg[-A_n^1\frac{2\mu n}{r^2}\left((n-1)\,H_n^{(1)}(k_pr)-k_prH_{n+1}^{(1)}(k_pr)\right)-\\
&\qquad A_n^2\frac{2\mu}{r^2}\left(\left(n^2-n-\frac{1}{2}k_s^2r^2\right)H_n^{(1)}(k_sr)+k_srH_{n+1}^{(1)}(k_sr)\right)-\\
&\qquad 2A_n^3\mu\frac{n}{r}\left(k_pH_n^{(2)'}(k_pr)-\frac{1}{r}H_n^{(2)}(k_pr)\right)+\\
&\qquad A_n^4\mu\left(-\frac{n^2}{r^2}H_n^{(2)}(k_sr)+\frac{1}{r}k_sH_n^{(2)'}(k_sr)-k_s^2H_n^{(2)''}(k_sr)\right)\Bigg]\sin(n\theta)\\
&=i\omega\rho v_s\sum_{n=0}^{+\infty}\Bigg[-A_n^1\frac{n}{r}H_n^{(1)}(k_pr)-A_n^2k_sH_n^{(1)'}(k_sr)-\\
&\qquad A_n^3\frac{n}{r}H_n^{(2)}(k_pr)-A_n^4k_sH_n^{(2)'}(k_sr)\Bigg]\sin(n\theta).
\end{aligned} \tag{A.21}$$

Since n represents modes of Fourier's serie, we compute the coefficients $\mathbf{A}_n^j$, $j=1,4$ by solving the following system at each Fourier mode n, since $\mathbf{C}_n$ is inversible

$$\mathbf{C}_n\mathbf{A}_n=\mathbf{B}_n, \tag{A.22}$$

where $\mathbf{C}_n=\begin{pmatrix}\mathbf{C}_n(:,1) & \mathbf{C}_n(:,2) & \mathbf{C}_n(:,3) & \mathbf{C}_n(:,4)\end{pmatrix}$

with $$\mathbf{C}_n(:,1) = \begin{pmatrix} k_p H_n^{(1)'}(k_p a) \\ -\frac{n}{a} H_n^{(1)}(k_p a) \\ \left(\left(n^2 - n - \frac{1}{2}k_p^2 b^2\right) H_n^{(1)}(k_p b) + k_p b H_{n+1}^{(1)}(k_p b)\right) - i\omega^2\rho\frac{b^2}{2\mu} H_n^{(1)'}(k_p b) \\ -n\left(\left(n-1\right) H_n^{(1)}(k_p b) - k_p b H_{n+1}^{(1)}(k_p b)\right) + i\omega\rho v_s n \frac{b}{2\mu} H_n^{(1)}(k_p b) \end{pmatrix},$$

$$\mathbf{C}_n(:,2) = \begin{pmatrix} \frac{n}{a} H_n^{(1)}(k_s a) \\ -k_s H_n^{(1)'}(k_s a) \\ n\left(\left(n-1\right) H_n^{(1)}(k_s b) - k_s b H_{n+1}^{(1)}(k_p b)\right) - i\omega\rho v_p n \frac{b}{2\mu} H_n^{(1)}(k_s b) \\ -\left(\left(n^2 - n - \frac{1}{2}k_s^2 b^2\right) H_n^{(1)}(k_s b) + k_s b H_{n+1}^{(1)}(k_s b)\right) + i\omega^2\rho\frac{b^2}{2\mu} H_n^{(1)'}(k_s b) \end{pmatrix},$$

$$\mathbf{C}_n(:,3) = \begin{pmatrix} k_p H_n^{(2)'}(k_p a) \\ -\frac{n}{a} H_n^{(2)}(k_p a) \\ \left(-\left(\left(k_s^2 - 2k_p^2\right) H_n^{(2)}(k_p b) + 2k_p^2 H_n^{(2)''}(k_p b)\right) - i\omega^2\rho H_n^{(2)'}(k_p b)\right)\frac{b^2}{2} \\ -nb\left(k_p H_n^{(2)'}(k_p b) - \frac{1}{b} H_n^{(2)}(k_p b)\right) + i\omega\rho v_s n \frac{b}{2\mu} H_n^{(2)}(k_p b) \end{pmatrix},$$

$$\mathbf{C}_n(:,4) = \begin{pmatrix} \frac{n}{a} H_n^{(2)}(k_s a) \\ -k_s H_n^{(2)'}(k_s a) \\ nb\left(\frac{-1}{b} H_n^{(2)}(k_s b) + k_s H_n^{(2)'}(k_s b)\right) - i\omega\rho v_p n \frac{b}{2\mu} H_n^{(2)}(k_s b) \\ \left(\left(-\frac{n^2}{b^2} H_n^{(2)}(k_s b) + \frac{1}{b} k_s H_n^{(2)'}(k_s b) - k_s^2 H_n^{(2)''}(k_s b)\right) + i\omega^2\rho\frac{1}{\mu} H_n^{(2)'}(k_s b)\right)\frac{b^2}{2} \end{pmatrix},$$

$$\mathbf{A}_n = \begin{pmatrix} A_n^1 \\ A_n^2 \\ A_n^3 \\ A_n^4 \end{pmatrix}, \qquad \mathbf{B}_n = \begin{pmatrix} -\varepsilon_n i^n k_p J_n'(k_p a) \\ \frac{n}{a}\varepsilon_n i^n J_n(k_p a) \\ 0 \\ 0 \end{pmatrix}.$$

B Analytical solution of the elastic solid scatterer problem

Like in the previous section, we recall here the analytical solution in the form of Fourier series of the elastic disk-shaped solid scatterer problem. The displacement field u is represented with the help to two potentials ϕ and ψ

$$u = \nabla\phi + (-\mathbf{e_z}) \times \nabla\psi, \tag{B.1}$$

where, in the case of a circle, like the domain Ω_a, we refer to figure 4.26 for the domains $\Omega, \Omega_a, \Omega_b$

$$\begin{aligned}\phi = \phi_3 &= \sum_{n=0}^{+\infty} A_n^3 J_n(k_p r)\cos(n\theta),\\ \psi = \psi_3 &= \sum_{n=0}^{+\infty} A_n^4 J_n(k_s r)\sin(n\theta),\end{aligned}$$

and in the case of a ring like Ω_b

$$\begin{aligned}\phi = \phi_1 + \phi_2 &= \sum_{n=0}^{+\infty} A_n^1 H_n^{(1)}(k_p r)\cos(n\theta) + \sum_{n=0}^{+\infty} A_n^5 H_n^{(2)}(k_p r)\cos(n\theta),\\ \psi = \psi_1 + \psi_2 &= \sum_{n=0}^{+\infty} A_n^2 H_n^{(1)}(k_s r)\sin(n\theta) + \sum_{n=0}^{+\infty} A_n^6 H_n^{(2)}(k_s r)\sin(n\theta).\end{aligned}$$

$\mathbf{e_z}$ is the third vector of the cartesian basis. $k_p = \dfrac{\omega}{v_p}$ et $k_s = \dfrac{\omega}{v_s}$. $H_n^{(1)}$ represents the Hankel's function of first kind defined such as

$$H_n^{(1)}(x) = J_n(x) + iY_n(x), \tag{B.2}$$

with J_n et Y_n Bessel's functions respectively of first and second kind. $H_n^{(2)}$ is the Hankel's function of second kind defined such as

$$H_n^{(2)}(x) = J_n(x) - iY_n(x). \tag{B.3}$$

In polar coordinates, we get

$$\nabla\phi = \frac{\partial\phi}{\partial r}\mathbf{e_r} + \frac{1}{r}\frac{\partial\phi}{\partial\theta}\mathbf{e}_\theta,$$

$$(-\mathbf{e_z}) \times \nabla\psi = \frac{1}{r}\frac{\partial\psi}{\partial\theta}\mathbf{e_r} - \frac{\partial\psi}{\partial r}\mathbf{e}_\theta.$$

It follows that

$$u = u_r\mathbf{e_r} + u_\theta\mathbf{e}_\theta, \tag{B.4}$$

where $\quad u_r = \dfrac{\partial\phi}{\partial r} + \dfrac{1}{r}\dfrac{\partial\psi}{\partial\theta} \quad$ and $\quad u_\theta = \dfrac{1}{r}\dfrac{\partial\phi}{\partial\theta} - \dfrac{\partial\psi}{\partial r}.$

Since polar vectors $\mathbf{e_r}$ and $\mathbf{e}_\theta$ are defined in cartesian basis by $(\cos\theta, \sin\theta)^t$ and $(-\sin\theta, \cos\theta)^t$ respectively, we obtain the components of the displacement field in the cartesian basis

$$\left\{\begin{array}{lcl} u_x &=& u_r\cos\theta - u_\theta\sin\theta,\\ u_z &=& u_r\sin\theta + u_\theta\cos\theta.\end{array}\right. \tag{B.5}$$

Then, in Ω_a, the components of displacement field u_3 are written

$$\left\{\begin{array}{lcl} u_{3x} & = & u_{3r}\cos\theta - u_{3\theta}\sin\theta, \\ u_{3z} & = & u_{3r}\sin\theta + u_{3\theta}\cos\theta, \end{array}\right. \tag{B.6}$$

where

$$u_{3r} = \sum_{n=0}^{+\infty}\left[A_n^3 k_p J_n'(k_p r) + \frac{n}{r}A_n^4 J_n(k_s r)\right]\cos(n\theta),$$

$$u_{3\theta} = \sum_{n=0}^{+\infty}\left[-A_n^3 \frac{n}{r} J_n(k_p r) - A_n^4 k_s J_n'(k_s r)\right]\sin(n\theta).$$

In Ω_b, the components of displacement field u_1 are written

$$\left\{\begin{array}{lclcc} u_{12x} & = & u_{1x}+u_{2x} & = & u_{1r}\cos\theta - u_{1\theta}\sin\theta + u_{2r}\cos\theta - u_{2\theta}\sin\theta \\ & & & = & (u_{1r}+u_{2r})\cos\theta - (u_{1\theta}+u_{2\theta})\sin\theta, \\ u_{12z} & = & u_{1z}+u_{2z} & = & u_{1r}\sin\theta + u_{1\theta}\cos\theta + u_{1r}\sin\theta + u_{1\theta}\cos\theta \\ & & & = & (u_{1r}+u_{2r})\sin\theta + (u_{1\theta}+u_{2\theta})\cos\theta, \end{array}\right. \tag{B.7}$$

where

$$u_{1r} = \sum_{n=0}^{+\infty}\left[A_n^1 k_p H_n^{(1)'}(k_p r) + \frac{n}{r}A_n^2 H_n^{(1)}(k_s r)\right]\cos(n\theta),$$

$$u_{1\theta} = \sum_{n=0}^{+\infty}\left[-A_n^1 \frac{n}{r} H_n^{(1)}(k_p r) - A_n^2 k_s H_n^{(1)'}(k_s r)\right]\sin(n\theta),$$

$$u_{2r} = \sum_{n=0}^{+\infty}\left[A_n^5 k_p H_n^{(2)'}(k_p r) + \frac{n}{r}A_n^6 H_n^{(2)}(k_s r)\right]\cos(n\theta),$$

$$u_{2\theta} = \sum_{n=0}^{+\infty}\left[-A_n^5 \frac{n}{r} H_n^{(2)}(k_p r) - A_n^6 k_s H_n^{(2)'}(k_s r)\right]\sin(n\theta),$$

so we get

$$u_{12r} = \sum_{n=0}^{+\infty}\left[A_n^1 k_p H_n^{(1)'}(k_p r) + \frac{n}{r}A_n^2 H_n^{(1)}(k_s r) + A_n^5 k_p H_n^{(2)'}(k_p r) + \frac{n}{r}A_n^6 H_n^{(2)}(k_s r)\right]\cos(n\theta),$$

$$u_{12\theta} = \sum_{n=0}^{+\infty}\left[-A_n^1 \frac{n}{r} H_n^{(1)}(k_p r) - A_n^2 k_s H_n^{(1)'}(k_s r) - A_n^5 \frac{n}{r} H_n^{(2)}(k_p r) - A_n^6 k_s H_n^{(2)'}(k_s r)\right]\sin(n\theta).$$

Derivatives of Hankel's function are determined by the following reccurence relations

$$H_n^{(1)'}(x) = \left\{\begin{array}{ll} -H_{n+1}^{(1)}(x) & \text{for } n = 0, \\ -H_{n+1}^{(1)}(x) + \dfrac{n}{x}H_n^{(1)}(x) & \text{for } n > 0, \end{array}\right.$$

$$H_n^{(2)'}(x) = \left\{\begin{array}{ll} -H_{n+1}^{(2)}(x) & \text{for } n = 0, \\ H_{n-1}^{(2)}(x) - \dfrac{n}{x}H_n^{(2)}(x) & \text{for } n > 0. \end{array}\right.$$

In the same way, the derivative of the Bessel's function of first kind is

$$J_n'(x) = \begin{cases} -J_{n+1}(x) & \text{for } n = 0, \\ -J_{n+1}(x) + \dfrac{n}{x} J_n(x) & \text{for } n > 0. \end{cases}$$

Using these definitions we rewrite u_{ir} and $u_{i\theta}$, $i = 12, 3$

$$u_{3r} = \sum_{n=0}^{+\infty} \left[A_n^3 k_p \left(-J_{n+1}(k_p r) + \frac{n}{k_p r} J_n(k_p r) \right) + \frac{n}{r} A_n^4 J_n(k_s r) \right] \cos(n\theta), \tag{B.8}$$

$$u_{3\theta} = \sum_{n=0}^{+\infty} \left[-A_n^3 \frac{n}{r} J_n(k_p r) - A_n^4 k_s \left(-J_{n+1}(k_s r) + \frac{n}{k_s r} J_n(k_s r) \right) \right] \sin(n\theta), \tag{B.9}$$

$$\begin{aligned} u_{12r} = \sum_{n=0}^{+\infty} \Bigg[& A_n^1 k_p \left(-H_{n+1}^{(1)}(k_p r) + \frac{n}{k_p r} H_n^{(1)}(k_p r) \right) + \frac{n}{r} A_n^2 H_n^{(1)}(k_s r) + \\ & A_n^5 k_p \left(H_{n-1}^{(2)}(k_p r) - \frac{n}{k_p r} H_n^{(2)}(k_p r) \right) + \frac{n}{r} A_n^6 H_n^{(2)}(k_s r) \Bigg] \cos(n\theta), \end{aligned} \tag{B.10}$$

$$\begin{aligned} u_{12\theta} = \sum_{n=0}^{+\infty} \Bigg[& -A_n^1 \frac{n}{r} H_n^{(1)}(k_p r) - A_n^2 k_s \left(-H_{n+1}^{(1)}(k_s r) + \frac{n}{k_s r} H_n^{(1)}(k_s r) \right) - \\ & A_n^5 \frac{n}{r} H_n^{(2)}(k_p r) - A_n^6 k_s \left(H_{n-1}^{(2)}(k_s r) - \frac{n}{k_s r} H_n^{(2)}(k_s r) \right) \Bigg] \sin(n\theta). \end{aligned} \tag{B.11}$$

In order to determine coefficients A_n^i, $i = 1, .., 6$, we use boundary conditions. We get

$$\begin{cases} u_{12} + u^{inc} & = & u_3 \\ \underline{\underline{\sigma}}_{12}\mathbf{n} + \underline{\underline{\sigma}}^{inc}\mathbf{n} & = & \underline{\underline{\sigma}}_3\mathbf{n} \end{cases} \qquad \text{on } \Gamma_a, \tag{B.12}$$

$$\underline{\underline{\sigma}}_{12}\mathbf{n} = v_p \left(v_{12} \cdot \mathbf{n} \right) \mathbf{n} + v_s \left(v_{12} \cdot \mathbf{t} \right) \mathbf{t} \qquad \text{on } \Gamma_b. \tag{B.13}$$

We refer to figure 4.26 for the definition of boundaries Γ_a and Γ_b.

u^{inc} is the displacement field of the incident wave described by

$$u^{inc} = \nabla \phi^{inc} + (-\mathbf{e_z}) \times \nabla \psi^{inc},$$

with $\psi^{inc} = 0$ and

$$\phi^{inc} = \sum_{n=0}^{+\infty} \varepsilon_n i^n J_n(k_p r) \cos(n\theta),$$

where $\varepsilon_n = \begin{cases} 1 & \text{if } n = 0 \\ 2 & \text{if } n \geq 1 \end{cases}$.

In summary, we have

$$\begin{aligned} u^{inc} &= \frac{\partial \phi^{inc}}{\partial r} \mathbf{e_r} + \frac{1}{r} \frac{\partial \phi^{inc}}{\partial \theta} \mathbf{e}_\theta \\ &= \sum_{n=0}^{+\infty} \varepsilon_n i^n \cos(n\theta) k_p J_n'(k_p r) \mathbf{e_r} + \sum_{n=0}^{+\infty} \frac{-n}{r} \varepsilon_n i^n J_n(k_p r) \sin(n\theta) \mathbf{e}_\theta, \end{aligned} \tag{B.14}$$

The free surface condition on Γ_a is given by

$$\left\{\begin{array}{lcl} \sigma_{rr_{12}} + \sigma_{rr}^{inc} & = & \sigma_{rr_3}, \\ \sigma_{r\theta_{12}} + \sigma_{r\theta}^{inc} & = & \sigma_{r\theta_3}, \end{array}\right. \tag{B.15}$$

and the absorbing condition on Γ_b by

$$\left\{\begin{array}{lcl} \sigma_{rr_{12}} & = & i\omega v_p u_{12r}, \\ \sigma_{r\theta_{12}} & = & i\omega v_s u_{12\theta}. \end{array}\right. \tag{B.16}$$

The components σ_{rr} and $\sigma_{r\theta}$ of $\underline{\underline{\sigma}}$ are expressed such as

$$\left\{\begin{array}{lcl} \sigma_{rr} & = & \sigma_{rr}^{\phi} + \sigma_{rr}^{\psi}, \\ \sigma_{r\theta} & = & \sigma_{r\theta}^{\phi} + \sigma_{r\theta}^{\psi}, \end{array}\right. \tag{B.17}$$

where

$$\begin{aligned} \sigma_{rr}^{\phi} &= \lambda\Delta\phi + 2\mu\frac{\partial^2\phi}{\partial r^2}, \\ \sigma_{rr}^{\psi} &= 2\mu\left[\frac{\partial}{\partial r}\left(\frac{1}{r}\frac{\partial\psi}{\partial\theta}\right)\right], \\ \sigma_{r\theta}^{\phi} &= 2\mu\left(\frac{1}{r}\frac{\partial^2\phi}{\partial\theta\partial r} - \frac{1}{r^2}\frac{\partial\phi}{\partial\theta}\right), \\ \sigma_{r\theta}^{\psi} &= \mu\left(\frac{1}{r^2}\frac{\partial^2\psi}{\partial\theta^2} - r\frac{\partial}{\partial r}\left(\frac{1}{r}\frac{\partial\psi}{\partial r}\right)\right). \end{aligned}$$

ϕ satisfies the Helmholtz equation

$$\Delta\phi = -k_p^2\phi,$$

so

$$\Delta\phi = -k_p^2\sum_{n=0}^{+\infty} A_n^h C_n(k_p r)\cos(n\theta), h = 1, 3 \text{ or} 5,$$

and $C_n(k_p r) = H_n^{(1)}(k_p r)$, $J_n(k_p r)$ or $H_n^{(2)}(k_p r)$. For $\underline{\underline{\sigma}}_1$ we get

$$\left\{\begin{array}{lcl} \sigma_{rr_1} & = & \displaystyle\sum_{n=0}^{+\infty}\left[A_n^1 k_p^2\left(\left(-\lambda - \frac{2\mu}{(k_p r)^2}\left(n + (k_p r)^2 - n^2\right)\right)H_n^{(1)}(k_p r) + 2\mu\frac{1}{k_p r}H_{n+1}^{(1)}(k_p r)\right) + \right. \\ & & \qquad \left. 2\mu A_n^2 \tfrac{n}{r}\left(\tfrac{-1}{r}\left(1-n\right)H_n^{(1)}(k_s r) - k_s H_{n+1}^{(1)}(k_s r)\right)\right]\cos(n\theta), \\ \sigma_{r\theta_1} & = & \displaystyle\mu\sum_{n=0}^{+\infty}\left[-2A_n^1\frac{n}{r}\left(-k_p H_{n+1}^{(1)}(k_p r) + \frac{n-1}{r}H_n^{(1)}(k_p r)\right) + \right. \\ & & \qquad \left. A_n^2 \tfrac{2}{r}\left(\tfrac{1}{r}\left(-n^2 + n + \tfrac{1}{2}(k_s r)^2\right)H_n^{(1)}(k_s r) - k_s H_{n+1}^{(1)}(k_s r)\right)\right]\sin(n\theta). \end{array}\right. \tag{B.18}$$

For $\underline{\underline{\sigma}}_2$

$$\left\{\begin{array}{lcl} \sigma_{rr_2} & = & \displaystyle\sum_{n=0}^{+\infty}\left[A_n^5 k_p^2\left(\left(-\lambda + \frac{2\mu}{(k_p r)^2}\left(n - (k_p r)^2 + n^2\right)\right)H_n^{(2)}(k_p r) - 2\mu\frac{1}{k_p r}H_{n-1}^{(1)}(k_p r)\right) + \right. \\ & & \qquad \left. 2\mu A_n^6 \tfrac{n}{r}\left(\tfrac{-1}{r}\left(1+n\right)H_n^{(2)}(k_s r) + k_s H_{n-1}^{(2)}(k_s r)\right)\right]\cos(n\theta). \\ \sigma_{r\theta_2} & = & \displaystyle\mu\sum_{n=0}^{+\infty}\left[-2A_n^5\frac{n}{r}\left(k_p H_{n-1}^{(2)}(k_p r) - \frac{n+1}{r}H_n^{(2)}(k_p r)\right) + \right. \\ & & \qquad \left. A_n^6 \tfrac{2}{r}\left(-\tfrac{1}{r}\left(n^2 + n - \tfrac{1}{2}(k_s r)^2\right)H_n^{(2)}(k_s r) + k_s H_{n-1}^{(2)}(k_s r)\right)\right]\sin(n\theta). \end{array}\right. \tag{B.19}$$

For $\underline{\underline{\sigma}}_3$

$$\left\{\begin{array}{lcl}
\sigma_{rr_3} & = & \displaystyle\sum_{n=0}^{+\infty}\left[A_n^3 k_p^2\left(\left(-\lambda-\frac{2\mu}{(k_p r)^2}\left(n+(k_p r)^2-n^2\right)\right)J_n(k_p r)+2\mu\frac{1}{k_p r}J_{n+1}(k_p r)\right)+\right. \\
& & \qquad\left. 2\mu A_n^4 \tfrac{n}{r}\left(\tfrac{-1}{r}\left(1-n\right)J_n(k_s r)-k_s J_{n+1}(k_s r)\right)\right]\cos(n\theta), \\
\sigma_{r\theta_3} & = & \displaystyle\mu\sum_{n=0}^{+\infty}\left[-2A_n^3\frac{n}{r}\left(-k_p J_{n+1}(k_p r)+\frac{n-1}{r}J_n(k_p r)\right)+\right. \\
& & \qquad\left. A_n^4 \tfrac{2}{r}\left(\tfrac{1}{r}\left(-n^2+n+\tfrac{1}{2}(k_s r)^2\right)J_n(k_s r)-k_s J_{n+1}(k_s r)\right)\right]\sin(n\theta).
\end{array}\right. \tag{B.20}$$

Finally for $\underline{\underline{\sigma}}^{inc}$

$$\left\{\begin{array}{lcl}
\sigma_{rr}^{inc} & = & \displaystyle\sum_{n=0}^{+\infty}\varepsilon_n i^n\left[\left(-\lambda k_p^2-2\mu\frac{1}{r^2}\left(n-n^2+(k_p r)^2\right)\right)J_n(k_p r)+2\mu\frac{k_p}{r}J_{n+1}(k_p r)\right]\cos(n\theta), \\
\sigma_{r\theta}^{inc} & = & \displaystyle\sum_{n=0}^{+\infty}\left[-2\mu\varepsilon_n i^n\frac{n}{r}\left(-\frac{1-n}{r}J_n(k_p r)-k_p J_{n+1}(k_p r)\right)\right]\sin(n\theta).
\end{array}\right. \tag{B.21}$$

For $r=a$ we have

$$\begin{aligned}
&\sum_{n=0}^{+\infty}\left[A_n^1 k_p\left(-H_{n+1}^{(1)}(k_p r)+\frac{n}{k_p r}H_n^{(1)}(k_p r)\right)+\frac{n}{r}A_n^2 H_n^{(1)}(k_s r)+\right. \\
&\qquad A_n^5 k_p\left(H_{n-1}^{(2)}(k_p r)-\frac{n}{k_p r}H_n^{(2)}(k_p r)\right)+\frac{n}{r}A_n^6 H_n^{(2)}(k_s r)- \\
&\qquad \left. A_n^3 k_p\left(-J_{n+1}(k_p r)+\frac{n}{k_p r}J_n(k_p r)\right)-\frac{n}{r}A_n^4 J_n(k_s r)\right]\cos(n\theta), \\
&=\sum_{n=0}^{+\infty}-\varepsilon_n i^n k_p\left(-J_{n+1}(k_p r)+\frac{n}{k_p r}J_n(k_p r)\right)\cos(n\theta),
\end{aligned}$$

$$\begin{aligned}
&\sum_{n=0}^{+\infty}\left[-A_n^1\frac{n}{r}H_n^{(1)}(k_p r)-A_n^2 k_s\left(-H_{n+1}^{(1)}(k_s r)+\frac{n}{k_s r}H_n^{(1)}(k_s r)\right)-A_n^5\frac{n}{r}H_n^{(2)}(k_p r)-\right. \\
&\qquad A_n^6 k_s\left(H_{n-1}^{(2)}(k_s r)-\frac{n}{k_s r}H_n^{(2)}(k_s r)\right)+A_n^3\frac{n}{r}J_n(k_p r)+ \\
&\qquad \left. A_n^4 k_s\left(-J_{n+1}(k_s r)+\frac{n}{k_s r}J_n(k_s r)\right)\right]\sin(n\theta) \\
&=\sum_{n=0}^{+\infty}\frac{n}{r}\varepsilon_n i^n J_n(k_p r)\sin(n\theta)
\end{aligned}$$

$$
\begin{aligned}
&\sum_{n=0}^{+\infty}\Bigg[A_n^1 k_p^2\left(\left(-\lambda-\frac{2\mu}{(k_pr)^2}\left(n+(k_pr)^2-n^2\right)\right)H_n^{(1)}(k_pr)+2\mu\frac{1}{k_pr}H_{n+1}^{(1)}(k_pr)\right)+\\
&\qquad 2\mu A_n^2\frac{n}{r}\left(\frac{-1}{r}\left(1-n\right)H_n^{(1)}(k_sr)-k_sH_{n+1}^{(1)}(k_sr)\right)+\\
&\qquad A_n^5 k_p^2\left(\left(-\lambda+\frac{2\mu}{(k_pr)^2}\left(n-(k_pr)^2+n^2\right)\right)H_n^{(2)}(k_pr)-2\mu\frac{1}{k_pr}H_{n-1}^{(1)}(k_pr)\right)+\\
&\qquad 2\mu A_n^6\frac{n}{r}\left(\frac{-1}{r}\left(1+n\right)H_n^{(2)}(k_sr)+k_sH_{n-1}^{(2)}(k_sr)\right)-\\
&\qquad A_n^3 k_p^2\left(\left(-\lambda-\frac{2\mu}{(k_pr)^2}\left(n+(k_pr)^2-n^2\right)\right)J_n(k_pr)+2\mu\frac{1}{k_pr}J_{n+1}(k_pr)\right)-\\
&\qquad 2\mu A_n^4\frac{n}{r}\left(\frac{-1}{r}\left(1-n\right)J_n(k_sr)-k_sJ_{n+1}(k_sr)\right)\Bigg]\cos(n\theta),\\
&=-\sum_{n=0}^{+\infty}\varepsilon_n i^n\left[\left(-\lambda k_p^2-2\mu\frac{1}{r^2}\left(n-n^2+(k_pr)^2\right)\right)J_n(k_pr)+2\mu\frac{k_p}{r}J_{n+1}(k_pr)\right]\cos(n\theta),
\end{aligned}
$$

$$
\begin{aligned}
&\mu\sum_{n=0}^{+\infty}\Bigg[-2A_n^1\frac{n}{r}\left(-k_pH_{n+1}^{(1)}(k_pr)+\frac{n-1}{r}H_n^{(1)}(k_pr)\right)+\\
&\qquad A_n^2\frac{2}{r}\left(\frac{1}{r}\left(-n^2+n+\frac{1}{2}(k_sr)^2\right)H_n^{(1)}(k_sr)-k_sH_{n+1}^{(1)}(k_sr)\right)-\\
&\qquad 2A_n^5\frac{n}{r}\left(k_pH_{n-1}^{(2)}(k_pr)-\frac{n+1}{r}H_n^{(2)}(k_pr)\right)+\\
&\qquad A_n^6\frac{2}{r}\left(-\frac{1}{r}\left(n^2+n-\frac{1}{2}(k_sr)^2\right)H_n^{(2)}(k_sr)+k_sH_{n-1}^{(2)}(k_sr)\right)+\\
&\qquad 2A_n^3\frac{n}{r}\left(-k_pJ_{n+1}(k_pr)+\frac{n-1}{r}J_n(k_pr)\right)-\\
&\qquad A_n^4\frac{2}{r}\left(\frac{1}{r}\left(-n^2+n+\frac{1}{2}(k_sr)^2\right)J_n(k_sr)-k_sJ_{n+1}(k_sr)\right)\Bigg]\sin(n\theta)\\
&=\sum_{n=0}^{+\infty}\left[-2\mu\varepsilon_n i^n\frac{n}{r}\left(-\frac{1-n}{r}J_n(k_pr)-k_pJ_{n+1}(k_pr)\right)\right]\sin(n\theta).
\end{aligned}
$$

n representing modes of Fourier's serie, we get for each Fourier mode n

$$
\begin{gathered}
\left[A_n^3k_pJ_n'(k_pr)+\frac{n}{r}A_n^4J_n(k_sr)-A_n^1k_pH_n^{(1)'}(k_pr)-\frac{n}{r}A_n^2H_n^{(1)}(k_sr)\right]\cos(n\theta)=\\
\varepsilon_n i^n\cos(n\theta)k_pJ_n'(k_pr),
\end{gathered}
\tag{B.22}
$$

$$
\begin{gathered}
\left[-A_n^3\frac{n}{r}J_n(k_pr)-A_n^4k_sJ_n'(k_sr)+A_n^1\frac{n}{r}H_n^{(1)}(k_pr)+A_n^2k_sH_n^{(1)'}(k_sr)\right]\sin(n\theta)=\\
\frac{-n}{r}\varepsilon_n i^nJ_n(k_pr)\sin(n\theta),
\end{gathered}
\tag{B.23}
$$

$$\begin{aligned}
&\Bigg[A_n^3\left(\left(\lambda+2\mu\right)k_p^2J_n^{''}(k_pr)+\lambda\left(\frac{1}{r}k_pJ_n^{'}(k_pr)-\frac{n^2}{r^2}J_n(k_pr)\right)\right)+\\
&2\mu A_n^4\frac{n}{r}\left(\frac{-1}{r}J_n(k_sr)+k_sJ_n^{'}(k_sr)\right)-\\
&A_n^1\left(\left(\lambda+2\mu\right)k_p^2H_n^{(1)''}(k_pr)+\lambda\left(\frac{1}{r}k_pH_n^{(1)'}(k_pr)-\frac{n^2}{r^2}H_n^{(1)}(k_pr)\right)\right)-\\
&2\mu A_n^2\frac{n}{r}\left(\frac{-1}{r}H_n^{(1)}(k_sr)+k_sH_n^{(1)'}(k_sr)\right)\Bigg]\cos(n\theta)\\
&=\varepsilon_n i^n\left[\left(\lambda+2\mu\right)k_p^2J_n^{''}(k_pr)+\lambda\left(\frac{1}{r}k_pJ_n^{'}(k_pr)-\frac{n^2}{r^2}J_n(k_pr)\right)\right]\cos(n\theta).
\end{aligned}\tag{B.24}$$

$$\begin{aligned}
&\Bigg[-2\mu A_n^3\frac{n}{r}\left(k_pJ_n^{'}(k_pr)-\frac{1}{r}J_n(k_pr)\right)+\\
&\mu A_n^4\left(-\frac{n^2}{r^2}J_n(k_sr)+\frac{1}{r}k_sJ_n^{'}(k_sr)-k_s^2J_n^{''}(k_sr)\right)+\\
&2\mu A_n^1\frac{n}{r}\left(k_pH_n^{(1)'}(k_pr)-\frac{1}{r}H_n^{(1)}(k_pr)\right)-\\
&\mu A_n^2\left(-\frac{n^2}{r^2}H_n^{(1)}(k_sr)+\frac{1}{r}k_sH_n^{(1)'}(k_sr)-k_s^2H_n^{(1)''}(k_sr)\right)\Bigg]\sin(n\theta)\\
&=-2\mu\varepsilon_n i^n\frac{n}{r}\left(k_pJ_n^{'}(k_pr)-\frac{1}{r}J_n(k_pr)\right)\sin(n\theta).
\end{aligned}\tag{B.25}$$

Since $k_p^2\left(\lambda+2\mu\right)=k_s^2\mu$, we replace λ by $\dfrac{k_s^2}{k_p^2}\mu-2\mu$ and rewriting equations (B.22) to (B.25) under matrix form, we finally get

$$\mathbf{C}_n\mathbf{A}_n=\mathbf{B}_n,\tag{B.26}$$

where

$$\mathbf{C}_n=\left(\begin{matrix}
-k_pH_n^{(1)'}(k_pa) & -\frac{n}{a}H_n^{(1)}(k_sa) & \dots\\
\frac{n}{a}H_n^{(1)}(k_pa) & k_sH_n^{(1)'}(k_sa) & \dots\\
-\left(k_s^2H_n^{(1)''}(k_pr)+\left(\frac{k_s^2}{k_p^2}-2\right)\left(\frac{1}{r}k_pH_n^{(1)'}(k_pr)-\frac{n^2}{r^2}H_n^{(1)}(k_pr)\right)\right) & -2\frac{n}{r}\left(\frac{-1}{r}H_n^{(1)}(k_sr)+k_sH_n^{(1)'}(k_sr)\right) & \dots\\
2\frac{n}{r}\left(k_pH_n^{(1)'}(k_pr)-\frac{1}{r}H_n^{(1)}(k_pr)\right) & -\left(-\frac{n^2}{r^2}H_n^{(1)}(k_sr)+\frac{1}{r}k_sH_n^{(1)'}(k_sr)-k_s^2H_n^{(1)''}(k_sr)\right) & \dots
\end{matrix}\right.$$

$$\left.\begin{matrix}
\dots & k_pJ_n'(k_pa) & \frac{n}{a}J_n(k_sa)\\
\dots & -\frac{n}{a}J_n(k_pa) & -k_sJ_n'(k_sa)\\
\dots & \left(k_s^2J_n^{''}(k_pr)+\left(\frac{k_s^2}{k_p^2}-2\right)\left(\frac{1}{r}k_pJ_n^{'}(k_pr)-\frac{n^2}{r^2}J_n(k_pr)\right)\right) & 2\frac{n}{r}\left(\frac{-1}{r}J_n(k_sr)+k_sJ_n^{'}(k_sr)\right)\\
\dots & -2\frac{n}{r}\left(k_pJ_n^{'}(k_pr)-\frac{1}{r}J_n(k_pr)\right) & \left(-\frac{n^2}{r^2}J_n(k_sr)+\frac{1}{r}k_sJ_n^{'}(k_sr)-k_s^2J_n^{''}(k_sr)\right)
\end{matrix}\right),$$

$$\mathbf{A}_n=\begin{pmatrix}A_n^1\\A_n^2\\A_n^3\\A_n^4\end{pmatrix},$$

$$\mathbf{B}_n = \begin{pmatrix} \varepsilon_n i^n k_p J_n'(k_p a) \\ -\dfrac{n}{a}\varepsilon_n i^n J_n(k_p a) \\ \varepsilon_n i^n \left(k_s^2 J_n^{''}(k_p r) + \left(\dfrac{k_s^2}{k_p^2} - 2 \right) \left(\dfrac{1}{r} k_p J_n^{'}(k_p r) - \dfrac{n^2}{r^2} J_n(k_p r) \right) \right) \\ -2\varepsilon_n i^n \dfrac{n}{r} \left(k_p J_n^{'}(k_p r) - \dfrac{1}{r} J_n(k_p r) \right) \end{pmatrix}.$$

Since $\mathbf{C}_n$ is inversible, we have to solve the following system to find coefficients $\mathbf{A}_n^j$, $j = 1, 6$

$$\mathbf{A}_n = \mathbf{C}_n^{-1} \mathbf{B}_n. \tag{B.27}$$

RESEARCH CENTRE
BORDEAUX – SUD-OUEST

200 avenue de la Vieille Tour
33405 Talence Cedex

Publisher
Inria
Domaine de Voluceau - Rocquencourt
BP 105 - 78153 Le Chesnay Cedex
inria.fr

ISSN 0249-6399